

Hadron production and quark-gluon plasma hadronization in Pb-Pb collisions at $\sqrt{s_{NN}} = 2.76$ TeVMichal Petráň,^{1,2} Jean Letessier,³ Vojtěch Petráček,² and Johann Rafelski^{1,4}¹*Department of Physics, The University of Arizona, Tucson, Arizona 85721, USA*²*Czech Technical University in Prague, Faculty of Nuclear Sciences and Physical Engineering*³*Laboratoire de Physique Théorique et Hautes Energies, Université Paris 6, Paris 75005, France*⁴*Theory Division of Physics Department, CERN, CH-1211 Geneva 23, Switzerland*

(Received 8 March 2013; revised manuscript received 16 August 2013; published 20 September 2013)

We show that all central rapidity hadron yields measured in Pb-Pb collisions at $\sqrt{s_{NN}} = 2.76$ TeV are well described by the chemical nonequilibrium statistical hadronization model (SHM), where the chemically equilibrated quark-gluon plasma source breaks up directly into hadrons. SHM parameters are obtained as a function of centrality of colliding ions, and we compare CERN Large Hadron Collider (LHC) results with Brookhaven National Laboratory Relativistic Heavy Ion Collider (RHIC) results. We predict yields of unobserved hadrons and address antimatter production. The physical properties of the quark-gluon plasma fireball particle source show universality of hadronization conditions at LHC and RHIC.

DOI: [10.1103/PhysRevC.88.034907](https://doi.org/10.1103/PhysRevC.88.034907)

PACS number(s): 25.75.Nq, 24.10.Pa, 12.38.Mh

I. INTRODUCTION AND MOTIVATION

Our interest in the multiparticle production process in ultra-relativistic heavy-ion collisions originates in the understanding that the transverse momentum integrated rapidity distributions are insensitive to the very difficult to fully characterize transverse evolution dynamics of the hot fireball source [1]. A successful description of central rapidity particle yields in a single freeze-out model [2,3] are used here to characterize the properties of the hadronizing quark-gluon-plasma (QGP) fireball. The QGP breakup, as modeled within the statistical hadronization model (SHM), assumes equal reaction strength in all hadron particle production channels. Therefore, the phase-space volume determines the hadron yields. SHM has been described extensively before and we refer the reader to SHARE manuals [4] for both further theoretical details and numerical methods. Here we apply SHM to study particle production in Pb-Pb collisions at $\sqrt{s_{NN}} = 2.76$ TeV (LHC2760), a new energy domain an order of magnitude higher than previously explored in Au-Au collisions at $\sqrt{s_{NN}} = 200$ GeV (RHIC200).

We begin by demonstrating that the chemical nonequilibrium SHM variant describes the experimental LHC-ion data with high accuracy. This finding disagrees with claims that SHM alone does not describe the particle multiplicity data obtained in relativistic heavy-ion collisions at LHC [5,6]. In the chemical nonequilibrium SHM approach, we allow quark pair yield parameter γ_q for light quarks, a feature we presented as a necessary model refinement for the past 15 yr [7–9]. We demonstrate the general model validity in our numerical approach by showing correspondence of chemical equilibrium SHM results with other fits to the LHC data. This demonstrates that several SHM programs, which had years to mature and evolve, are compatible in their data tables of hadronic resonance mass spectra and decay patterns. However, only our extended SHARE code includes advanced features, such as chemical nonequilibrium of all quark yields, differentiation of up and down quarks, evaluation of fireball physical properties, and the capability to constrain the fit by imposing physical properties on the particle source.

To demonstrate that our chemical nonequilibrium SHM works at LHC, we show in the left-hand side of Fig. 1 our fit to the 0%–20% centrality data, shown in the second column of Table I, recently presented and studied by the experiment ALICE [5,6]. Only in this one instance we consider the relatively wide centrality trigger of 0%–20% to compare directly with the earlier analysis effort. As can be seen in the left-hand side of Fig. 1, our nonequilibrium SHM approach describes these data with $\chi^2/\text{ndf} = 9.5/9 \simeq 1$. We see in the Fig. 1(a) inset that the chemical equilibrium SHM works poorly, $\chi^2/\text{ndf} = 64/11 \simeq 6$, which is the same finding and conclusion as in Refs. [5,6].

While the equilibrium SHM disagrees at LHC across many particle yields the most discussed data point is the $p/\pi = 0.046 \pm 0.003$ ratio [6], a point we study in more detail in Sec. III B. Our work shows that the inability of the equilibrium SHM alone to fit the experimental value of the p/π ratio does not mean that all variants of SHM do not describe particle production in heavy-ion collisions at LHC. One of the key findings of this work is that the chemical nonequilibrium SHM variant without any additional posthadronization evolution provides an excellent description of all data. We also argue that the present-day hybrid models, that is, models that combine SHM results with posthadronization hadron yield evolution, need to address key features of the data such as quasiconstancy of the p/π ratio as a function of centrality of the heavy-ion collision and the abundance of multistrange baryons.

The chemical nonequilibrium results for the 5%–10% centrality bin (containing interpolated data, open symbols) is shown for comparison in the right-hand panel of Fig. 1. The fit has the same set of particles as the 0%–20% centrality bin; however, we must fit here three ratios for which data are directly (or by interpolation) available, and we use a more recent set of proton, pion, and kaon data. Definition of the model and some technical details about how we obtain results seen in Fig. 1 follow below; the fitted data are shown in the fourth column of Table I. The Fig. 1(c) shows the SHM parameters and χ^2 for all three variants. Comparing the SHM parameters on left- and right-hand sides of Fig. 1 we see a large

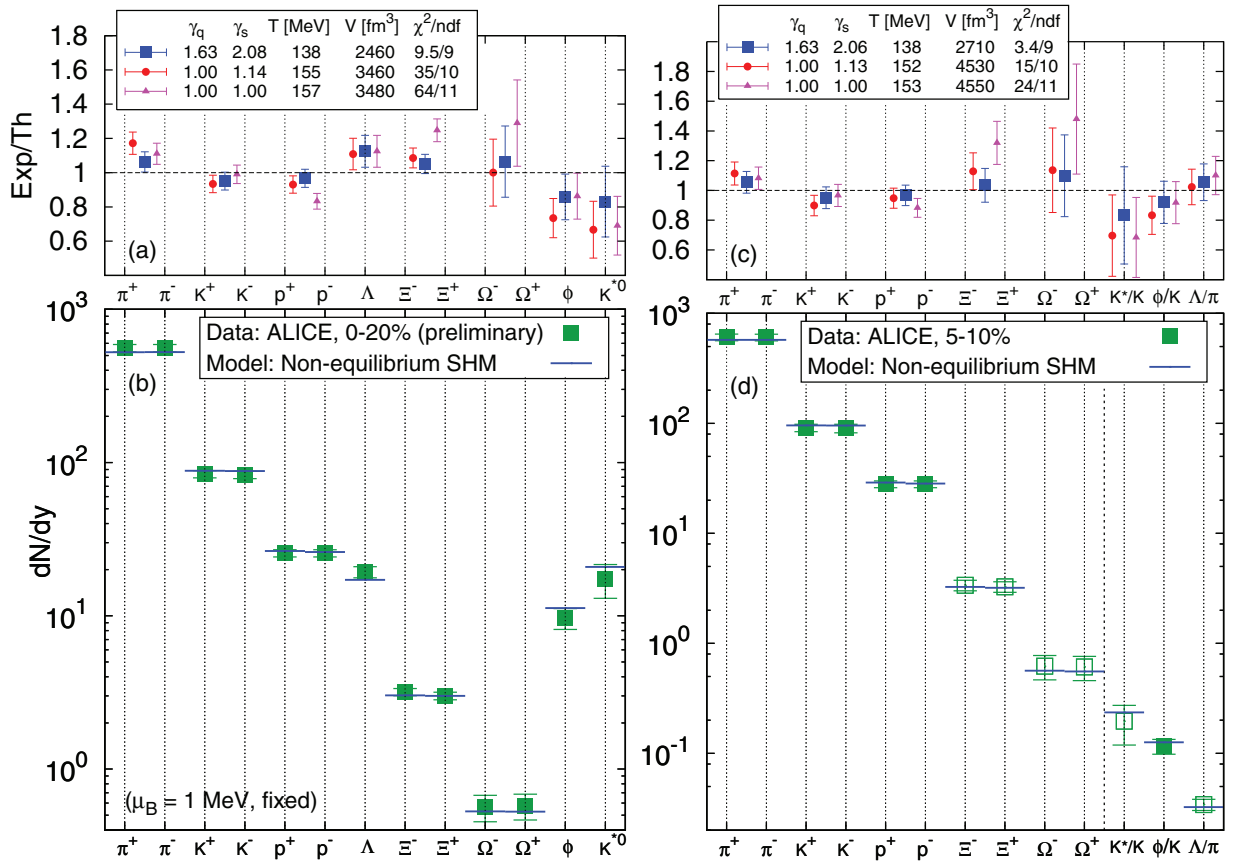


FIG. 1. (Color online) SHM fit to experimental data measured by the ALICE experiment in Pb-Pb collisions at $\sqrt{s_{NN}} = 2.76$ TeV for 0%–20% centrality [panels (a) and (b) on the left-hand side] and for 1/4 of this range, 5%–10% [panels (c) and (d) on the right-hand side]. The input set of particle types is the same as can be seen in particle listing on the ordinates of panels (b) and (d); in panel (d) also particle yield ratios are used. In the panels (b) and (d) comparison of SHM chemical nonequilibrium fit (horizontal line) with data is shown. The experimental data are shown as solid squares; in the panel (d) the interpolated experimental data are shown with open symbols (see Appendix for details). Panels (a) and (c) show the ratio of model values to experimental data for the three SHM variants and present the key parameter values for chemical nonequilibrium (solid squares), chemical semiequilibrium (solid circles), and chemical equilibrium (solid triangles). For readability, antiparticles are omitted in panels (a) and (c).

change in V expected for different centralities. We see that use of finer centrality binning and more mature data sample reduces χ^2 for all SHM variants.

As Fig. 1 shows and we discuss below in detail, the chemical nonequilibrium SHM works perfectly at LHC, resulting in a high confidence level. This could be predicted considering prior CERN Super Proton Synchrotron (SPS) and RHIC data analyses [10–12], which strongly favor chemical nonequilibrium variant of SHM. Moreover, the chemical nonequilibrium SHM has a dynamical physical foundation in sudden breakup of a QGP fireball, we are not aware of a dynamical origin of the simple chemical equilibrium SHM because no dynamical computation of relativistic heavy-ion scattering achieves the chemical equilibrium condition without introduction of an unknown particle, cross sections, etc. Furthermore, as we discuss in Sec. III C, we obtain hadronization universality across a wide collision energy range: Comparing RHIC62 with LHC2760 we show that the fireball source of particles is nearly identical and consistent with chemically equilibrated QGP fireball. Given this result, the chemical nonequilibrium

SHM variant is validated across a wide energy range, while the chemical equilibrium SHM [13–18] is invalidated by the LHC data and this conclusion can be extended across different reaction energies because there is no reason why a model should work only sporadically.

We have now shown that the chemical nonequilibrium is the necessary ingredient in the SHM approach to the process of hadronization of a QGP fireball. The nonequilibrium SHM was proposed when first strange hadron multiplicity results were interpreted more than 20 yr ago [19]. The yield of strange hadrons indicated that the number of quark pairs present had to be modified by a factor γ_s ; the source of strangeness is not populating the final-state hadrons with the yields expected from the hadronic chemical equilibrium, a point of view widely accepted today. At SPS energies, for which this model was originally conceived, the production of strangeness did not yet saturate the QGP phase space; that is, strangeness was out of chemical equilibrium both in the QGP fireball source with $\gamma_s^Q < 1$ and thus also in the final hadronic state with also $\gamma_s^H < 1$. The distinction of QGP as

TABLE I. Table of data points we use as input for SHM fits; hadron yields (dN/dy) and ratios at midrapidity $|y| < 0.5$ for different centralities. The header of the table defines the centrality bins in three different ways. Centrality as a function of N_{part} is taken from [29]. Errors are combined systematic and statistical errors added in quadratures where systematic errors are, in general, dominant and statistical errors are negligible. Values in brackets are interpolated data. See Appendix for details about data sources and how data are rebinned.

Centrality	0%–20%	0%–5%	5%–10%	10%–20%	20%–30%	30%–40%	40%–50%	50%–60%	60%–70%	70%–80%
$\langle N_{\text{part}} \rangle$	308	382.8	329.7	260.5	186.4	128.9	85.0	52.8	30.0	15.8
$dN_{\text{ch}}/d\eta$		1601 ± 60	1294 ± 49	966 ± 37	649 ± 23	426 ± 15	261 ± 9	149 ± 6	76 ± 4	35 ± 2
π^+	562 ± 36	733 ± 54	606 ± 42	455 ± 31	307 ± 20	201 ± 13	124 ± 8	71 ± 5	37 ± 2	17.1 ± 1.1
π^-	560 ± 34	732 ± 52	604 ± 42	453 ± 31	306 ± 20	200 ± 13	123 ± 8	71 ± 4	37 ± 2	17.0 ± 1.1
K^+	84 ± 5.4	109 ± 9	91 ± 7	68 ± 5	46 ± 4	30 ± 2	18.3 ± 1.4	10.2 ± 0.8	5.1 ± 0.4	2.3 ± 0.2
K^-	84 ± 5.7	109 ± 9	90 ± 8	68 ± 6	46 ± 4	30 ± 2	18.1 ± 1.5	10.2 ± 0.8	5.1 ± 0.4	2.3 ± 0.2
K^{*0}	17.3 ± 4.2									
$K^{0*}/K \cdot 10^3$		(188 ± 98)	(196 ± 77)	(209 ± 54)	(227 ± 59)	(247 ± 64)	(269 ± 70)	(295 ± 77)	(326 ± 85)	(361 ± 94)
p	25.9 ± 1.6	34 ± 3	28 ± 2	21.0 ± 1.7	14.4 ± 1.2	9.6 ± 0.8	6.1 ± 0.5	3.6 ± 0.3	1.9 ± 0.2	0.90 ± 0.08
\bar{p}	26.0 ± 1.8	33 ± 3	28 ± 2	21.1 ± 1.8	14.5 ± 1.2	9.7 ± 0.8	6.2 ± 0.5	3.7 ± 0.3	2.0 ± 0.2	0.93 ± 0.09
ϕ	9.6 ± 1.4									
$\phi/K \cdot 10^3$		109 ± 20	116 ± 18	117 ± 17	128 ± 19	120 ± 20	123 ± 18	123 ± 19	119 ± 18	119 ± 21
Λ	19.3 ± 2.0									
$\Lambda/\pi \cdot 10^3$		(33.3 ± 3.9)	(34.2 ± 4.0)	(35.3 ± 4.1)	(36.4 ± 4.3)	(37.0 ± 4.3)	(37.1 ± 4.4)	(36.8 ± 4.3)	(36.0 ± 4.2)	(34.7 ± 4.1)
$\Xi^- \cdot 10^2$	323 ± 35	(397 ± 44)	(337 ± 37)	(258 ± 28)	(176 ± 19)	(116 ± 13)	(71.6 ± 7.9)	(40.7 ± 4.5)	(19.6 ± 2.2)	(7.5 ± 0.8)
$\Xi^+ \cdot 10^2$	304 ± 33	(382 ± 42)	(327 ± 36)	(253 ± 28)	(176 ± 19)	(118 ± 13)	(73.7 ± 8.1)	(42.3 ± 4.7)	(20.3 ± 2.2)	(7.1 ± 0.8)
$\Omega^- \cdot 10^2$	57 ± 10	(78 ± 19)	(62 ± 16)	(45 ± 11)	(29 ± 7)	(18 ± 4)	(10 ± 3)	(5.4 ± 1.4)	(2.5 ± 0.6)	(1.0 ± 0.3)
$\Omega^+ \cdot 10^2$	58 ± 11	(76 ± 18)	(61 ± 15)	(45 ± 11)	(29 ± 7)	(18 ± 4)	(10 ± 3)	(5.5 ± 1.4)	(2.5 ± 0.6)	(1.0 ± 0.3)

the initial and the final hadron phase-space domain for γ_s was also modeled [20]. It is important to always remember that hadron phase-space nonequilibrium can arise from a QGP fireball with strangeness in chemical equilibrium, because, in general, the QGP and hadron phase-space strangeness densities are greatly different. Moreover, it is quite possible that a not-yet-in-chemical equilibrium QGP, which is the higher density phase, produces an equilibrated hadron yield. This can, however, happen only accidentally and variation of reaction energy or collision centrality shows this.

Another nonequilibrium parameter γ_c , similar to γ_s , was introduced very soon after γ_s to control the charm final-state phase space [20], and it has been widely adopted in consideration of a strong charm yield overabundance above chemical hadron gas equilibrium. Note that both strangeness and charm flavors are therefore assumed to have been produced in a separate and independent process before hadronization, and note further that each of the production mechanisms, in this case, is different, with charm originating in first parton collisions and strangeness being also abundantly produced in secondary thermalized gluon fusion reactions. At the end of QGP expansion, these available and independently established strangeness and charm particle supplies are distributed into available final-state phase-space cells, which is the meaning of SHM in a nutshell.

The full chemical nonequilibrium is introduced by means of the parameter $\gamma_q \neq 1$. This situation arises when the source of hadrons disintegrates faster than the time necessary to reequilibrate the yield of light quarks present. The two-pion correlation data provide experimental evidence that favors a rapid breakup of QGP with a short time of hadron production [21] and thus favors very fast, or sudden, hadronization

[22,23]. In this situation, a similar chemical nonequilibrium approach must be applied to the light quark abundance, introducing the light quark phase-space occupancy γ_q . This proposal made for the high-energy SPS data [7,8], helped improve the understanding of RHIC200 hadron rapidity yield results [10], and allowed a consistent interpretation of these data across the full energy range at SPS and RHIC200 [11].

For more than a decade we have made continued effort to show that a high-quality (low χ^2) and simple (no need for hybrid models) description of hadron abundances emerges using chemical nonequilibrium SHM. However, the recognition of the necessity of light quark (u, d) chemical nonequilibrium, i.e., $\gamma_q \neq 1$, remains sparse, despite the consistency of this approach with the two-pion correlation results, which provides additional evidence for fast hadronization [21]. The recent steady advances of lattice QCD [24–27] favors QGP hadronization at a temperature below the once-preferred $T_c = 165$ MeV temperature. As already noted, the equilibrium SHM variant imposing $\gamma_q = 1$ light quark chemical equilibrium [13–18] produces (relatively dense) particle chemical freeze-out near $T = 155$ MeV. Such freeze-out assumes, on one hand, in the present context a relatively high QGP hadronization temperature and, on the other hand, requires as a complement an “afterburner” describing further reaction evolution of some particles. As we argue in Sec. III B, such a “hybrid” model does not result in a viable description of the precise ALICE experimental data.

This is the case since the LHC2760 experimental environment has opened a new experimental opportunity to investigate in detail the SHM hadron production model. Precise particle tracking near the interaction vertex in the ALICE experiment removes the need for off-line corrections of weak interaction

decays, and at the same time vertex tracking is enhancing the efficiency of track identification, increasing considerably the precision of particle yield measurement [5,28]. All data used in the present work were obtained in this way by the LHC-ALICE experiment for Pb-Pb collisions at $\sqrt{s_{NN}} = 2.76$ TeV, limited to the central unit of rapidity interval $-0.5 < y < 0.5$. The experimental particle yield results are reported in different collision centrality bins according to the geometric overlap of colliding nuclei, with the “smallest,” e.g., 0%–5% centrality bin corresponding to the nearly fully overlapping geometry of the colliding nuclei. The collision geometry model [29] relates the centrality trigger to the number of participating nucleons N_{part} , which we use as our preferred centrality variable in what follows.

Section II presents our general method and approach to the particle multiplicity data analysis. Following a brief summary of the SHM methods in Sec. II A, we describe in Sec. II B our centrality study of particle production based on the following data: For the 0%–20% centrality bin, we obtain the preliminary data from [5,28]. For the centrality study of particle production, we present in Table I the final yields of π^\pm , K^\pm , and p^\pm as presented in Ref. [30]. The preliminary ratio ϕ/K is from Ref. [31]; these seven data points are binned in the same centrality bins and are used as presented. However, several other particle types require rebinning with interpolation and, at times, extrapolation, which is further discussed in Appendix. The (preliminary) data input into this rebinning for K^{*0}/K^- and for $2\Lambda/(\pi^- + \pi^+)$ are also taken from Ref. [31]. Using the preliminary enhancement factors of Ξ^- , Ξ^+ , Ω^- , Ω^+ shown in Refs. [32,33], combined with yields of these particles for p - p reactions at $\sqrt{s_{NN}} = 7$ TeV as presented in Ref. [34], we obtain the required yield input; see Appendix. In Sec. II C, we present particles both fitted and predicted by SHM, including antimatter clusters.

In Sec. III, we discuss the key physics outcome of the fits, i.e., the resulting SHM parameters as a function of centrality. We compare to the equilibrium approach in Sec. III A. We discuss the differences seen between the SHM variants and compare our results to our analysis of Au-Au collisions at $\sqrt{s_{NN}} = 62.4$ GeV at RHIC62, because it is a system we analyzed in detail recently [12]. We obtain the bulk physical properties—energy density, entropy density, and pressure—as a function of centrality in Sec. III C, where we also address strangeness and entropy yields. This study is made possible because all SHM parameters are determined with minimal error in consideration of the precise experimental particle multiplicity result. We discuss how our results relate to the lattice-QCD study of QGP properties in Sec. III D. We close our paper with a short summary and discussion of all results in Sec. IV.

II. SHM AND PARTICLE PRODUCTION

A. Generalities

We use here SHM implementation within the SHARE program [4]. The SHM describes the yields of particles given the chemical freeze-out temperature T and overall normalization dV/dy (as the experimental data are available as dN/dy). We account for the small asymmetry between

particles and antiparticles by fugacity factors λ_q , λ_s and the light quark asymmetry λ_{I3} ; see Ref. [4]. We further note that it is not uncommon to present the particle-antiparticle asymmetry employing the baryochemical and strangeness chemical potentials defined by

$$\mu_B = 3T \ln \lambda_q \quad \text{and} \quad \mu_S = T \ln(\lambda_q/\lambda_s), \quad (1)$$

the “inverse” definition of μ_S with reference to λ_s has historical origin and is a source of frequent error.

For each value of λ_q , strangeness fugacity λ_s is evaluated by imposing the strangeness conservation requirement $\langle s \rangle - \langle \bar{s} \rangle \simeq 0$. From now on, we omit the bra-kets indicating grand canonical average of the corresponding summed particle yield. The isospin fugacity factor λ_{I3} is constrained by imposing the charge per baryon ratio present in the initial nuclear-matter state at the initial instant of the collision. We achieve this objective by fitting these conservation laws along with particle yield data, using the following form:

$$\frac{s - \bar{s}}{s + \bar{s}} = 0.00 \pm 0.01, \quad (2)$$

$$\frac{Q - \bar{Q}}{B - \bar{B}} = 0.38 \pm 0.02. \quad (3)$$

We believe that implementing conservation laws as data points with errors accounts for the possibility that particles escape asymmetrically from the acceptance domain.

In the LHC2760 energy regime, there is near symmetry of particle and antiparticle sector; thus, the chemical potentials are hard to quantify. Therefore, the two constraints Eqs. (2) and (3) alone were not sufficient to achieve smooth behavior of the chemical potentials as a function of centrality. We therefore impose as a further constraint a constant baryon number stopping per participating nucleon in the midrapidity region in the following form:

$$\frac{b - \bar{b}}{N_{\text{part}}} = 0.0054 \pm 1\%. \quad (4)$$

We selected condition (4) because this was the variable that emerged in unconstrained fits as being most consistent. The value we selected is our estimate based on convergence without constraint to this value at several centralities. The alternative to this approach would have been to take a constant value of μ_B across centrality. While this produces a good-enough fit as well, this approach was poorly motivated: The unconstrained fit results produced a rather random-looking distribution of μ_B across centrality and thus did not present any evidence pointing towards a specific choice for μ_B . While the actual method of fixing matter-antimatter asymmetry is extraneous to the main thrust of this paper, the value of μ_B is of some relevance when considering predictions for antinuclei which we present further below.

Our considerations include the already described phase-space occupancy parameters γ_s and γ_q , where the light quarks $q = u, d$ are not distinguished. We do not study γ_c here; in other words, we do not include in the present discussion the charm degree of freedom. We note that there is no current experimental p_\perp -integrated charmed hadron yield information available from Pb-Pb collisions at LHC. The integration of the

phase-space distribution is not yet possible owing to uncertain low transverse momentum yields.

Thus, in the LHC2760 energy domain, we have at most $7 - 3 = 4$ independent statistical model parameters: seven parameters— dV/dy , T , λ_q , λ_s , λ_{I3} , γ_q , and γ_s —constrained by the three conditions—Eqs. (2)–(4)—to describe within SHM approach many very precise data points spanning in yield across centrality more than 5 orders of magnitude. We show for comparison results obtained setting arbitrarily $\gamma_q = 1$ (chemical semiequilibrium fit, comprising 6 parameters – 3 constraints) and then $\gamma_q = \gamma_s = 1$ (chemical equilibrium fit, 5 parameters – 3 constraints).

Absolute yields of hadrons are proportional to one power of γ_q for each constituent light quark (or antiquark) and one power of γ_s for each strange quark (or antiquark). For example, γ_q enters nonstrange baryon-to-meson ratios in the following manner:

$$\frac{\text{baryon}(qqq)}{\text{meson}(q\bar{q})} \propto \frac{\gamma_q^3}{\gamma_q^2} F(T, m_{\text{baryon}}, m_{\text{meson}}), \quad (5)$$

where q stands for either u or d quark and F is the integral over all particle momenta of the phase-space distribution at freeze-out temperature. We always use exact form of relativistic phase-space integrals. For strange hadrons, we must replace γ_q with γ_s for each constituent s (and/or \bar{s}) quark. Experimentally measured light baryon-to-meson ratios (such as p/π) strongly depend on the value of γ_q in a fit. Similarly, $\Lambda(qqs)/\pi(q\bar{q}) \propto \gamma_s$ is very sensitive to the value of γ_s .

The value of γ_q is bound by appearance of a pion condensate which corresponds to a singularity in the pion Bose-Einstein distribution function reached at the condition

$$\gamma_q^{\text{crit}} = \exp\left(\frac{m_{\pi^0}}{2T}\right). \quad (6)$$

This numerically works out for $T = 138$ – 160 MeV to be in the range $\gamma_q^{\text{crit}} = 1.63$ – 1.525 . However, there is a much more lax limit on the range of γ_s ; strangeness can increase very far before a particle condensation phenomenon limit is reached for the η meson.

B. Centrality study

The input hadron yield data used in the fit to the 0%–20% centrality bin is shown in the second column of Table I. The fit to this data set for the case of chemical equilibrium, where one forces $\gamma_s = \gamma_q = 1$, was done in Ref. [28], choosing a fixed value $\mu_B = 1$ MeV. In a first step, we compare to these results and follow this approach. However, we consider it necessary to apply strangeness and charge per baryon conservation by fitting Eqs. (2) and (3) as two additional data points determining the corresponding values of chemical parameters μ_S , μ_{I3} , a procedure omitted in the report Ref. [28], where $\mu_S = \mu_{I3} = 0$ was set. Naturally, the effect of this improvement is minimal, but it assures physical consistency. We show the values of χ_{total}^2 in Fig. 2; see the large open symbols. The wider range of N_{part} corresponding to the centrality bin 0%–20% is shown in Fig. 2 as horizontal uncertainty bars.

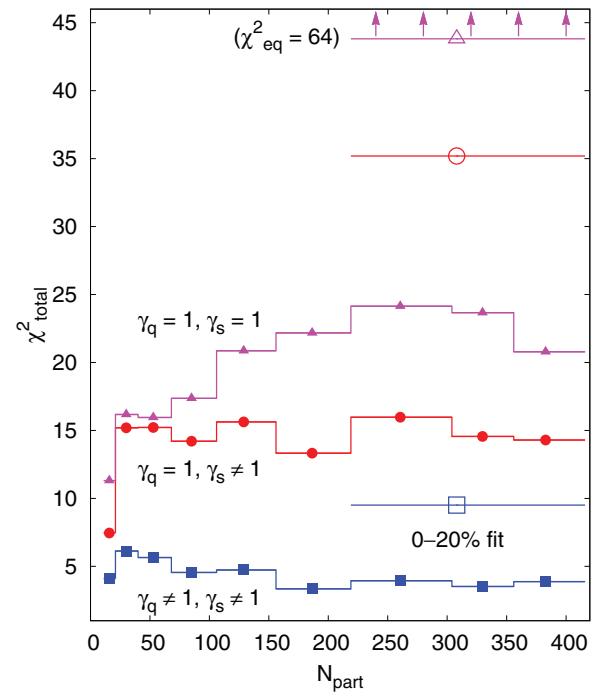


FIG. 2. (Color online) Total χ^2 as a function of centrality, as indicated in the figure, for the total equilibrium ($\gamma_q = \gamma_s = 1$, $\text{ndf} = 11$), for the semiequilibrium ($\gamma_q = 1$, $\gamma_s \neq 1$, $\text{ndf} = 10$), and for chemical nonequilibrium ($\gamma_q \neq 1$, $\gamma_s \neq 1$, $\text{ndf} = 9$) SHM. Open symbols represent the total χ^2 for the 0%–20% centrality bin depicted in Figs. 1(a) and 1(b). The number of degrees of freedom for the three cases, respectively, is $\text{ndf} = 11, 10, 9$. (The value of equilibrium SHM in the 0%–20% bin has been shifted down by 20 to fit in the figure.)

In our detailed centrality-dependent analysis, we use data in nine finer centrality bins, which we show in the 3rd to 11th and last column of Table I. The bins are classified according to the average number of participants N_{part} as a measure of centrality. This is a model value originating in the experimentally measured pseudorapidity density of charged particles $dN_{\text{ch}}/d\eta$ [29], which we state in the third row of Table I. We consider the consistency in Fig. 3: The experimentally measured $dN_{\text{ch}}/d\eta$ in the relevant participant bins [30] is shown by square symbols, as well as our SHM results for rapidity density of charged particles dN_{ch}/dy emerging directly from QGP (i.e., primary charged hadrons) and the final yield of charged hadrons, as triangles, fed by the decay of hadronic resonances. In all cases, we show, in Fig. 3, the yield per pair of interacting nucleons using the model value N_{part} . While the primary charged hadron rapidity yield (solid circles) is well below the pseudorapidity density $dN_{\text{ch}}/d\eta$ of charged hadrons (solid squares), the final rapidity yield dN_{ch}/dy after strong decays (solid triangles) is well above it. This result, $dN_{\text{ch}}/dy > dN_{\text{ch}}/d\eta$, is consistent with dynamical models describing the momentum spectra, which account for the production of charged particles that are not identified by experiments [1].

In Fig. 3, we see that about 50% of charged hadronic particles are produced by strong decays of heavier resonances. We show, in Fig. 4, the ratio of primarily produced yield to

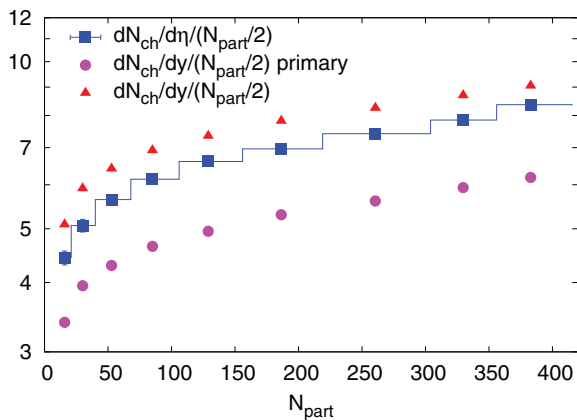


FIG. 3. (Color online) Experimental charged-particle yield pseudorapidity density $dN/d\eta$ (blue squares), and geometric model relating to charged-particle rapidity density dN/dy of only primary particles (violet circles) and including feed from strongly decaying resonances (red triangles) per participant pairs $N_{\text{part}}/2$.

the total yield for different particle species in the expected range of hadronization temperatures. The dominant fraction, almost 80%, of π and p yield originates from decaying resonances. This result demonstrates the difficulty that one encounters in the interpretation of transverse momentum spectra which must account for the decays and is thus, in a profound way, impacted by collective flow properties of many much heavier hadrons [1–3]. Conversely, this means that one can perform a convincing analysis of transverse momentum distribution only for hadrons, which do not have a significant feed from resonance decays, such as Ω or ϕ . This finding is the reason why we study the p_{\perp} integrated yields of hadrons in exploration of the physics of the fireball particle source. Moreover, we believe that “blast-wave” model fits to p_{\perp} hadron spectra are only meaningful for the Ω or ϕ hadrons.

The centrality binning, which differs for the different particles considered, requires us to use several interpolated and even some slightly extrapolated experimental results, which

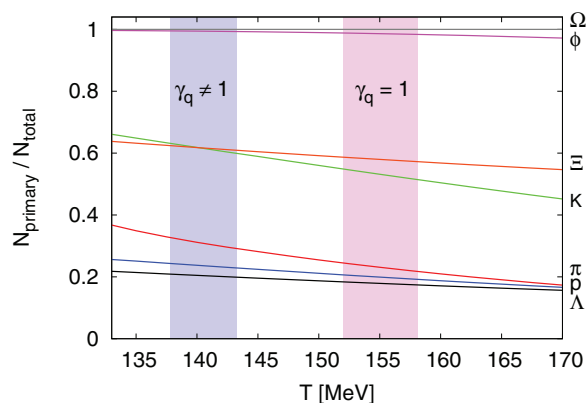


FIG. 4. (Color online) Fraction of primary hadrons produced, normalized by their final yield, which consists of primary produced hadrons and the feed from strong decaying resonances, for particles indicated in the right margin, as a function of hadronization temperature in single freeze-out model.

procedure we discuss in depth below and in Appendix. In our fits, we choose to use the centrality bins with the largest number of directly determined experimental data, minimizing the potential error originating in our multipoint interpolation. A few particles appear more than once in our data set (as a yield and/or in a ratio). However, to prevent duplicity, we always fit every particle measured just once.

To show that the finer centrality binning matters, we have already shown the 5%–10% centrality bin [which contains only close extrapolation; see open symbols in Figs. 1(b) and 1(d)]. The fit has the same set of particles as the 0%–20% centrality bin seen in Figs. 1(a) and 1(c), however, some of these particles enter the finer binned fit in ratios. If the outcome of the fit as a function of centrality is even a small variation in fitted parameters (other than normalization, i.e., volume), we expect and we find that the 5%–10% centrality bin, which describes a much smaller participant N_{part} range, leads to smaller χ^2 compared to the wide 0%–20% case. However, the stability of the fit parameters implies that much of the improvement is attributable to the revision in the input data set. The 0%–20% fit is based on preliminary data [28], whereas 5%–10% includes more recent final data [30] (see Appendix for details). For chemical nonequilibrium SHM an improvement of χ^2 by a factor of 4 is found for both preliminary 0%–20% and more recent final data set in 5%–10% bin as compared to chemical equilibrium SHM, thus favoring our simple nonequilibrium hadronization model.

We perform a fit to the entire data set with all three SHM approaches and compare the resulting χ^2 as a function of N_{part} in Fig. 2. The solid squares represent the chemical nonequilibrium SHM ($\gamma_q \neq 1$, $\gamma_s \neq 1$), the solid circles represent the semiequilibrium SHM ($\gamma_q = 1$, $\gamma_s \neq 1$), and solid triangles represent the full equilibrium SHM ($\gamma_q = \gamma_s = 1$). The range of centrality is indicated by the horizontal bars. Considering most central bins, we note in Fig. 2 that allowing $\gamma_q \neq 1$ can reduce the total χ^2 of the fit by more than a factor of 3 compared to semiequilibrium and more than a factor of 5 comparing full nonequilibrium with full equilibrium.

As a last step, we verify if there is a special value of the parameter γ_q of particular importance. To this end, we have evaluated the χ^2/ndf of the fit as a function of a given fixed γ_q within a range $\gamma_q \in (0.95, \gamma_q^{\text{crit}})$. This χ^2 profile curves, seen in Fig. 5, all pass $\gamma_q = 1$ smoothly; therefore, $\gamma_q = 1$ has no special importance for the SHM. However, fits to data in all centralities decrease in χ^2 as γ_q increases; they all point to best-fit value of γ_q near the critical value of Bose-Einstein condensation given by Eq. (6).

The most peripheral bin (70%–80%, $N_{\text{part}} = 15.8$) analyzed here requires further discussion as it shows in Fig. 5 a different behavior and in particular a considerably lower χ^2 when $\gamma_q \rightarrow 1$. For this peripheral centrality bin the procedure we use to interpolate data of Ξ , Ω , Λ/π , and K^*/K assigns a narrow peripheral centrality range to these experimental data points obtained for a much greater centrality domain spanning a participant range which is considerably wider. This can be a problem because within the wider centrality range the experimental results change rapidly with participant number. Therefore, our extrapolation towards the edge of the experimental data centrality range may introduce a fit

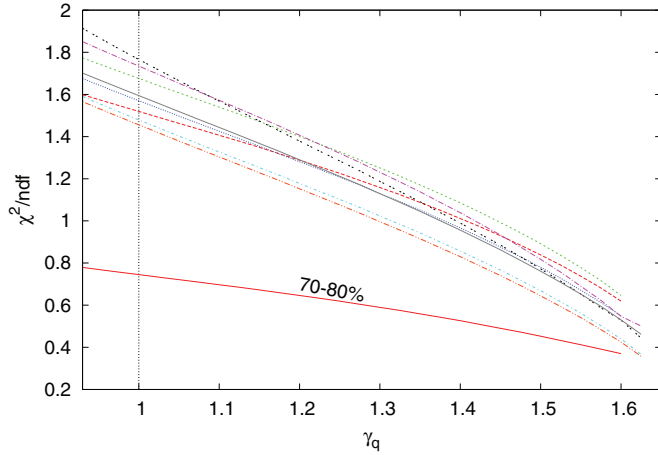


FIG. 5. (Color online) χ^2/ndf profile as a function of γ_q for all studied centralities.

aberration; here it happens that the created data are less incompatible with equilibrium SHM variants when $\gamma_q \rightarrow 1$. We do not believe that there is any issue with the result of the fit for $\gamma_q \rightarrow 1.6$ we discuss in this work. A different approach, in which we recombine the bins rather than interextrapolate, was presented in Ref. [35].

C. Particle yields

We compare input to the resulting particle yields graphically in Fig. 6. We fit 13 particles, counting antiparticles, which in the figure cannot be visually distinguished as an independent input or output data, and ratios Λ/π , K^*/K , and ϕ/K . For these ratios, the relevant yield outputs Λ , K^* , and ϕ are shown. Direct comparison of the input Λ/π , K^*/K , and ϕ/K ratios to the output is presented in Fig. 7; note that the ϕ/K ratio is available as an experimental data point in all centrality bins. The fitted output yields are stated also in the top portion of Table II, and ratios are given just below, allowing for comparison with the input values.

Our fit results appear as open circles in Fig. 6, at times completely overlaying the input data (solid symbols). For the Λ , the dotted line guides the eye, because the actual fit is to the ratio Λ/π shown in Fig. 7; no absolute Λ data are available. In the absence of absolute yields, only the open circles, i.e., the fitted values, are shown in Fig. 6. A similar situation arises with ϕ and K^* , where data are not available, but we fit ϕ/K and K^{0*}/K . One can see that SHM-generated results follow closely both the experimental data available and the interpolation dashed lines for each particle and that each interpolation curve passes through the experimental data points shown as full symbols or, at worst, the error bars if these are larger than the symbol.

Even so, we note in Fig. 6 that our interpolation for Ω shows a slightly different systematic shape (dashed line) compared the fit results (open symbols) or the behavior of the other particles. In other words, we see that other particles “predict” the yield of Ω that follows the centrality dependence of other particles, while the four data points lead to a centrality distribution that is slightly different. More precise Ω data will,

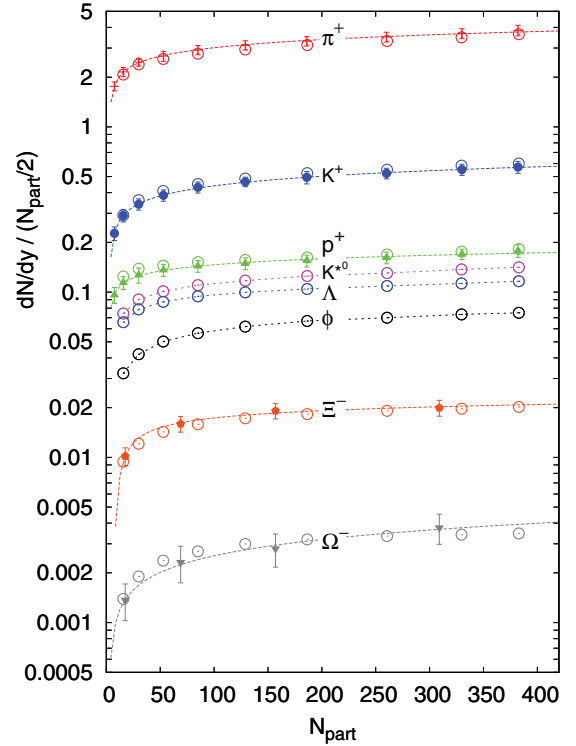


FIG. 6. (Color online) Solid symbols are the experimental data points. Open symbols represent the outcome for our chemical nonequilibrium SHM fit to LHC2760 as a function of centrality, i.e., N_{part} . Dashed lines are the outcome of our data interpolation of experimental yields available (see Appendix). Dotted lines connecting Λ , K^* , and ϕ SHM output values are presented to guide the eye; because ratios of these particles were used in our fit, the data are shown in Fig. 7.

without any doubt, offer a resolution to this slight tension in our interpolation. The hadron yields we find are also stated in Table II. Aside from the yields, we show there frequently

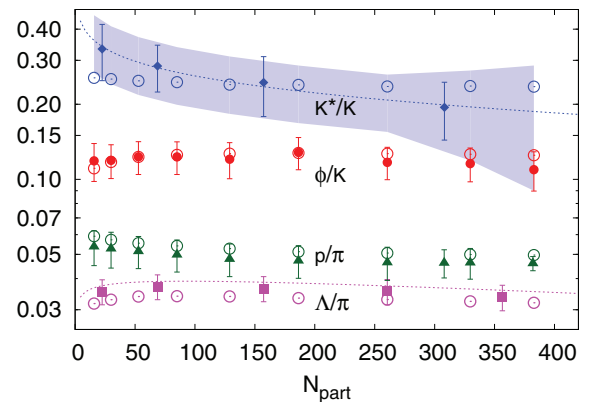


FIG. 7. (Color online) Solid symbols, experimental data with errors for K^*/K , ϕ/K , and Λ/π as a function of centrality, i.e., number of participants N_{part} . Lines are the interpolation (respectively, extrapolation) except for the case ϕ/K , where dotted line guides the eye. Open circles represent the resulting fit value for each ratio. The (blue) shaded band shows the error input used obtaining the interpolated values of K^*/K ratio.

TABLE II. Table of hadron yield output. The header of the table defines the centrality bins in three different ways. The top section of the table shows fitted yields dN/dy of hadrons entering the fit at LHC2760 obtained in the chemical nonequilibrium SHM. Next are three ratios that are actually included in the fit (rather than the yields of Λ , K^{0*} , ϕ), followed by the ratios of hadron yields that can be formed from the stated results, stated here for convenience of the reader. In the two lower sections of the table, there are predicted yields of yet-unmeasured hadrons, and at the very bottom we show predicted yields of light antinuclei scaled up by factor 1000 (and by 10^6 for antihelium). Note that yield of matter particles is nearly the same.

Centrality bin (N_{part})	0%–20%	0%–5%	5%–10%	10%–20%	20%–30%	30%–40%	40%–50%	50%–60%	60%–70%	70%–80%
dN_{ch}/dy	308	382.8	329.7	260.5	186.4	128.9	85.0	52.8	30.0	15.8
π^+	525	696	574	431	292	190	118	68.0	35.8	16.4
π^-	525	696	575	430	292	189	118	68.1	35.9	16.4
K^+	88.4	115	96.0	71.8	49.0	31.4	19.2	10.8	5.41	2.30
K^-	88.1	114	95.5	72.1	48.7	31.5	19.1	10.8	5.37	2.30
p	26.5	34.9	29.0	22.0	15.1	10.1	6.45	3.82	2.08	0.982
\bar{p}	26.1	34.2	28.4	21.6	14.8	9.89	6.30	3.72	2.02	0.953
K^{0*}	20.8	27.0	22.6	17.0	11.7	7.56	4.68	2.67	1.36	0.587
ϕ	11.2	14.4	12.1	9.12	6.23	3.99	2.40	1.33	0.632	0.255
Λ	17.2	22.3	18.6	14.2	9.73	6.43	4.00	2.31	1.18	0.520
Ξ^-	3.03	3.86	3.25	2.49	1.70	1.11	0.674	0.377	0.181	0.0745
$\bar{\Xi}^+$	3.00	3.80	3.22	2.43	1.68	1.08	0.664	0.371	0.179	0.0726
$\Omega^- 10^3$	529	663	561	435	297	193	115	62.6	28.5	11.0
$\bar{\Omega}^+ 10^3$	527	654	560	421	295	186	114	62.1	28.4	10.7
$\Lambda/\pi 10^3$	32.7	32.0	32.4	33.0	33.4	33.9	34.0	33.9	32.9	31.7
$K^{0*}/K 10^3$	236	235	237	236	239	240	245	248	252	255
$\phi/K 10^3$	127	125	126	127	128	127	125	123	117	111
$\phi/\pi^- 10^3$	21.4	20.6	21.0	21.2	21.4	21.1	20.3	19.5	17.6	15.6
$K^-/\pi^- 10^3$	168	165	166	167	167	167	162	158	150	141
$p/\pi^+ 10^3$	50.4	50.2	50.5	51.0	51.8	53.2	54.8	56.2	58.0	60.0
$\Xi/\pi 10^3$	5.76	5.55	5.65	5.79	5.84	5.86	5.71	5.53	5.06	4.55
$\Omega/\pi 10^3$	1.007	0.952	0.976	1.010	1.019	1.019	0.973	0.920	0.795	0.671
$K^{0*}/\pi 10^3$	39.6	38.8	39.3	39.5	40.0	39.9	39.7	39.2	37.8	35.9
p/K	0.300	0.303	0.302	0.306	0.309	0.322	0.336	0.354	0.385	0.426
η	61.0	79.7	66.3	49.8	33.9	21.9	13.4	7.64	3.90	1.72
$\rho(770)^0$	38.9	51.3	42.5	32.1	21.9	14.5	9.14	5.35	2.87	1.34
$\omega(782)^0$	35.1	46.4	38.4	29.0	19.8	13.1	8.28	4.85	2.61	1.22
$\Delta(1232)^{++}$	4.98	6.57	5.46	4.15	2.86	1.92	1.23	0.734	0.402	0.191
$\Sigma^*(1385)^-$	2.08	2.70	2.26	1.72	1.18	0.785	0.492	0.284	0.146	0.065
$\Lambda^*(1520)$	1.09	1.41	1.18	0.907	0.625	0.418	0.264	0.153	0.0795	0.0355
$\Xi^*(1530)^-$	1.02	1.30	1.09	0.84	0.58	0.378	0.230	0.129	0.0626	0.0258
${}^2\bar{\text{H}} 10^3$	74.7	98.1	81.9	62.6	43.6	29.4	19.5	11.8	6.53	3.16
${}^3\bar{\Lambda} 10^3$	0.478	0.601	0.506	0.397	0.279	0.191	0.128	0.0773	0.0415	0.0193
${}^3\bar{\text{H}} 10^3$	1.64	2.13	1.79	1.39	0.983	0.677	0.468	0.290	0.166	0.083
${}^3\bar{\text{He}} 10^3$	1.64	2.14	1.79	1.39	0.986	0.679	0.469	0.291	0.166	0.083
${}^4\bar{\text{He}} 10^6$	5.87	7.57	6.41	5.04	3.64	2.56	1.85	1.18	0.697	0.362

quoted ratios of particle yields; e.g., we find $p/\pi^+ \simeq 0.05$. We return to discuss this ratio in Sec. III B.

Figure 7 has the largest differences between theory and experiment. In case of the Λ/π ratio, we see a systematic within error bar underprediction at all centralities. For K^*/K , we see within the error bar a different slope of the fit as a function of centrality. The question can be asked if these differences of fit and results indicate some not-yet-understood physics contents. However, we are within the error bars and such data-fit difference must be expected and is allowed given a large data sample and potential for experimental refinement of these two preliminary data sets involving K^* and Λ . We recall

that at RHIC200, the K^*/K ratio was 10%–15% smaller and agrees with current ALICE results within the error margin [36]. We also note that we did not yet study how the charmed hadron decay particles influence the fit.

Predictions for the six hadron yields— η , ρ^0 , $\Delta(1232)^{++}$, $\Lambda^*(1520)$, $\Sigma^*(1385)^-$, $\Xi^*(1530)^0$ —are shown in Fig. 8 as a function of centrality; these results are stated in the lower portion of Table II. We further show five different species of (strange) antimatter, from antideuteron to anti- α , including antihypertriton, appropriately scaled to fit into Fig. 8. Our predictions of these composite objects should serve as a lower limit of their production rates: Fluctuation in the QGP

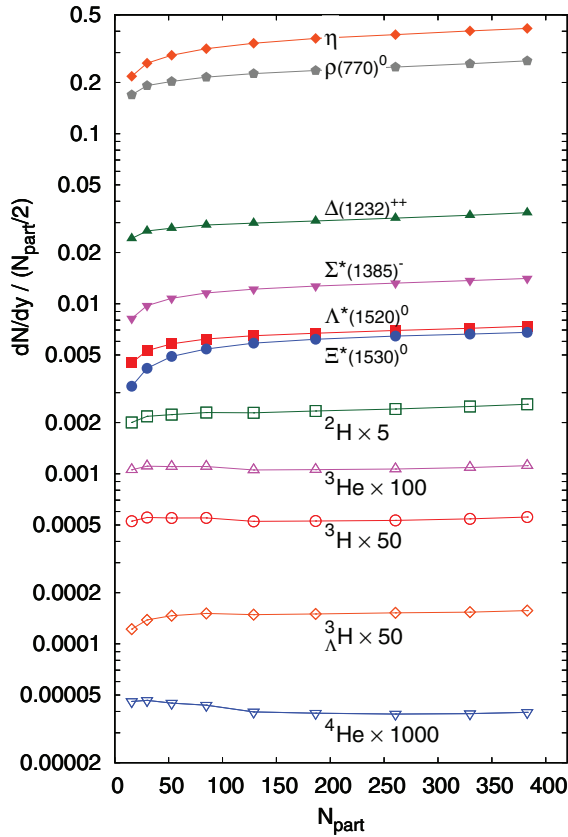


FIG. 8. (Color online) Particles predicted by the chemical nonequilibrium SHM fits. Predictions for hadron yields (solid symbols) are above antinuclei yield predictions (open symbols), which have been multiplied by suitable factors. Lines guide the eye; points are actual predictions for each of the nine centralities we analyzed.

homogeneity at hadronization and recombinant formation after hadronization may add contributions to the small SHM yield; see here the corresponding RHIC result [37].

III. PARTICLE SOURCE AND ITS PROPERTIES

A. Statistical parameters

In Fig. 9, we depict the LHC2760 statistical parameters as a function of collision centrality and compare these LHC2760 results with those we have obtained at RHIC62 [12], shown with open symbols. In all three panels of Fig. 9, we show parameter errors evaluated by SHAREV2 [4] employing the MINOS minimization routine. One can see that the parameter values for chemical nonequilibrium are defined better than for the case with $\gamma_q = 1$.

We present LHC2760 hadronization parameters for the nonequilibrium SHM case also in the top section of Table III. In Fig. 9(a), we see the particle source volume dV/dy , in Fig. 9(b) the chemical freeze-out temperature T , and in Fig. 9(c) the phase-space occupancies; the different variants are distinguished by superscripts “neq” (nonequilibrium, that is, $\gamma_q \neq 1, \gamma_s \neq 1$), “seq” (semiequilibrium, $\gamma_q = 1, \gamma_s \neq 1$), and “eq” (equilibrium, $\gamma_q = 1, \gamma_s = 1$). To compare with the

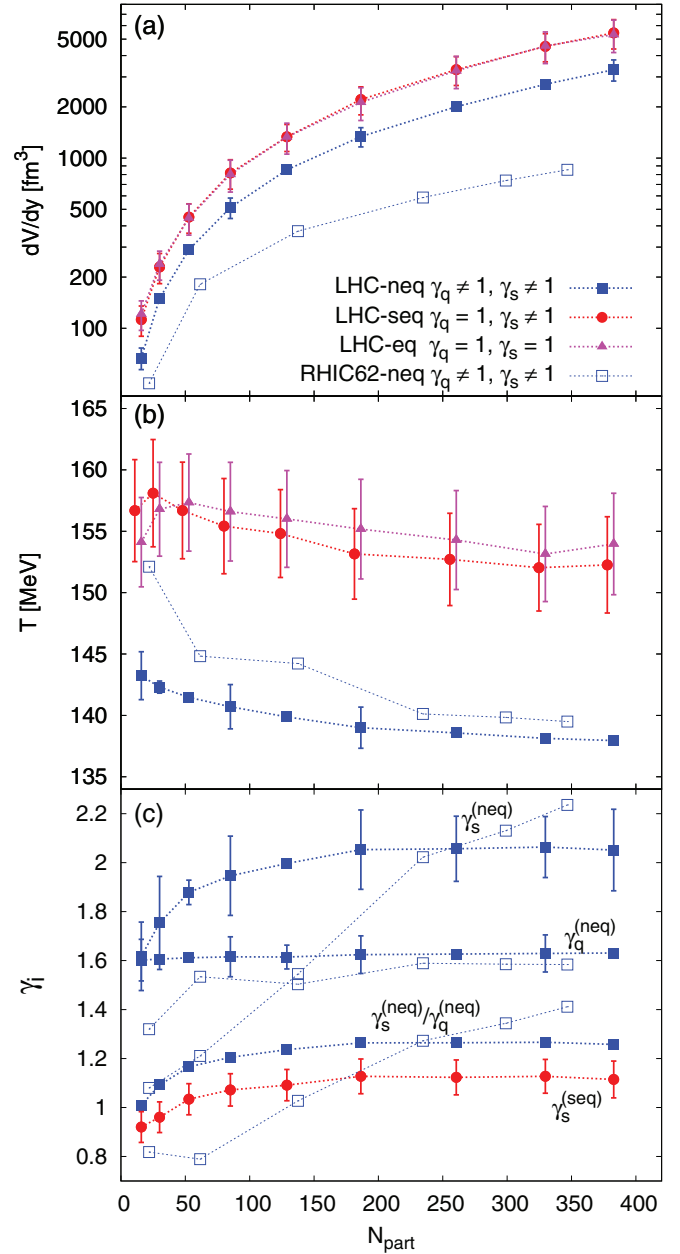


FIG. 9. (Color online) SHM parameters as a function of centrality, i.e., number of participants N_{part} , presented for the three different levels of chemical equilibrium, and compared to the chemical nonequilibrium SHM RHIC62 results (open symbols, dashed lines). All lines guide the eye. From top to bottom: (a) dV/dy (note that the volume for both equilibrium and semiequilibrium SHM variants is so close that symbols overlap); (b) T , the chemical freeze-out temperature (semiequilibrium symbols are offset to separate them from equilibrium); (c) phase-space occupancies $\gamma_s^{(\text{neq})}, \gamma_q^{(\text{neq})}$, and for comparison with equilibrium $\gamma_s^{(\text{seq})}$; we also present $\gamma_s^{(\text{neq})}/\gamma_q^{(\text{neq})}$.

semiequilibrium SHM variant, we show the ratio $\gamma_s^{(\text{neq})}/\gamma_q^{(\text{neq})}$, a ratio which helps to quantify the strangeness to light quark enhancement. This is to be directly compared with the semiequilibrium strangeness phase-space occupancy $\gamma_s^{(\text{seq})}$, given fixed $\gamma_q^{(\text{seq})} = 1$.

TABLE III. The top section shows chemical nonequilibrium SHM fit parameters dV/dy , T , γ_q , γ_s , and χ_{total}^2 with ndf (number data less number of parameters) obtained in each centrality bin. For error discussion, see text in Sec. III C. The bottom section presents fireball bulk properties in each bin: energy density ε , pressure P , entropy density σ , strangeness per entropy content s/S , entropy at LHC2760 compared to RHIC62, $S_{\text{LHC}}/S_{\text{RHIC}}$, and net baryon number per entropy ratio b/S .

Centrality (N_{part})	0%–20%	0%–5%	5%–10%	10%–20%	20%–30%	30%–40%	40%–50%	50%–60%	60%–70%	70%–80%
dV/dy (fm ³)	2463 ± 6	3304 ± 469	2715 ± 81	2003 ± 47	1337 ± 173	853.9 ± 5.9	512.2 ± 70.1	289.4 ± 5.5	149.8 ± 5.0	66.9 ± 9.7
T (MeV)	138.3 ± 0.0	138.0 ± 0.0	138.1 ± 0.0	138.6 ± 0.0	139.0 ± 1.7	139.9 ± 0.0	140.7 ± 1.8	141.5 ± 0.0	142.3 ± 0.5	143.2 ± 2.0
γ_q	1.63 ± 0.00	1.63 ± 0.00	1.63 ± 0.08	1.63 ± 0.00	1.62 ± 0.08	1.62 ± 0.05	1.62 ± 0.08	1.61 ± 0.00	1.61 ± 0.00	1.60 ± 0.09
γ_s	2.08 ± 0.00	2.05 ± 0.17	2.06 ± 0.13	2.06 ± 0.13	2.05 ± 0.16	2.00 ± 0.01	1.95 ± 0.16	1.88 ± 0.05	1.75 ± 0.19	1.62 ± 0.14
$\chi_{\text{total}}^2/\text{ndf}$	9.51/9	3.87/9	3.52/9	3.94/9	3.35/9	4.73/9	4.55/9	5.65/9	6.13/9	4.09/9
ε (GeV/fm ³)	0.462	0.453	0.457	0.467	0.476	0.487	0.505	0.516	0.521	0.527
P (MeV/fm ³)	78.5	77.1	77.7	79.1	80.5	82.3	85.1	86.8	87.9	89.2
σ (fm ⁻³)	3.20	3.14	3.17	3.23	3.28	3.36	3.46	3.53	3.56	3.60
s/S	0.0299	0.0295	0.0297	0.0297	0.0298	0.0294	0.0290	0.0284	0.0272	0.0257
$S_{\text{LHC}}/S_{\text{RHIC}}$	3.07	3.23	3.10	2.93	2.75	2.56	2.33	2.06	1.74	1.27
$b/S \times 10^4$	1.37	2.00	2.08	2.19	2.30	2.45	2.61	2.81	3.06	3.57

For the LHC2760 data, the SHM forcing chemical equilibrium of light quarks (i.e., $\gamma_q = 1$ with either $\gamma_s = 1$ or $\gamma_s \neq 1$) have a very similar volume dV/dy and similar chemical freeze-out T , as shown in Figs. 9(a) and 9(b), respectively, with nearly overlapping lines for dV/dy . In the nonequilibrium approach, dV/dy is reduced by about 20%–25% and the freeze-out temperature T by 10% compared to the equilibrium SHM variant. Compared to the RHIC62 results [12] (open symbols) the LHC2760 volume dV/dy is up to a factor 4 larger while the LHC hadronization temperature T is 2–5 MeV lower. Thus, given equal number of participants N_{part} at RHIC62 and LHC2760, the much larger particle multiplicity dN/dy requires in consideration of the universal hadronization condition [35] considerably increased transverse dimension of the fireball at the time of hadronization, which we find within our SHM interpretation of hadron production data. We understand this growth of particle multiplicity (and therefore volume) as being attributable to a greater transverse fireball expansion, driven by the greater initial energy density formed in a LHC2760 heavy-ion collision. This corresponds to a greater initial pressure necessary for the matter expansion to the same bulk hadronization conditions as already found at RHIC. The small but systematic decrease of the freeze-out temperature at LHC2760 compared to RHIC62 may be an indication of a greater supercooling caused by the more dynamical LHC expansion.

The freeze-out temperature T at LHC2760 decreases when considering more central collisions; see Fig. 9(b). In the hadronization scenario used in this work, this can be interpreted as being attributable to a deeper supercooling of the most central and most energetic collision systems. We can extrapolate the freeze-out temperature to $N_{\text{part}} = 0$ in the figure to set an upper limit on hadronization temperature at LHC2760, $T_{\text{had}} \rightarrow 145 \pm 4$ MeV, applicable to a small (transverse size) fireball. This, then, is the expected hadronization temperature without supercooling. Excluding, in Fig. 9(b), the most peripheral T -fit point for RHIC62, which does not have a good confidence level, we see that T at RHIC62 converges towards the same maximum value as we found at LHC2760,

thus confirming the determination of T_{had} as the common hadronization temperature without supercooling.

We show the phase-space occupancies γ_q, γ_s in Fig. 9(c). We note that the LHC2760 fit produces nearly a constant γ_q as a function of centrality. However, γ_s (and respectively γ_s/γ_q) decreases for more peripheral collisions towards unity, suggesting that these flavors approach the same level of chemical equilibrium for systems of small transverse size. A similar situation for peripheral collisions was observed for RHIC62. However, at RHIC62, we see a strong centrality dependence of γ_s and, hence, γ_s/γ_q . This rapid rise of the RHIC62 γ_s as a function of centrality can be attributed to the buildup of strangeness in QGP formed at RHIC62, which is imaged in the later produced strange hadron yield. Note that, omitting the most peripheral RHIC62 point, the peripheral γ_q is nearly the same as at LHC2760. The small difference can be attributed to the smaller allowed value of γ_q for the slightly higher value of T seen at RHIC62.

We have executed all our fits allowing for the presence of the chemical potentials [Eq. (1)] characterizing the slight matter-antimatter asymmetry present at LHC2760. The quality of the fit is not sufficiently improved including effectively one extra parameter (μ_B , because μ_S is fixed by strangeness conservation) to assure that the unconstrained results for μ_B are convincing. As mentioned in Sec. II A, we smooth the centrality dependence of μ_B by introducing baryon stopping fraction at midrapidity, that is, imposing Eq. (4) as an additional data point, a value that we saw a few times in the data without introducing this constraint. This constraint leads to the chemical potentials μ_B and μ_S presented in Fig. 10, with the baryochemical potential $1 \leq \mu_B \leq 2.3$ MeV and $\mu_S = 0.0 \pm 0.5$ MeV for all centralities, values an order of magnitude smaller than at RHIC62 and RHIC200. As we can see, even with the constraint, there are two centralities which do not agree with the trend set by the other seven data points.

Data shown in Fig. 10 are not defined well enough to argue that we see a decrease of baryochemical potential with increasing centrality, because this outcome could be the result of the bias we introduced. However, we think that

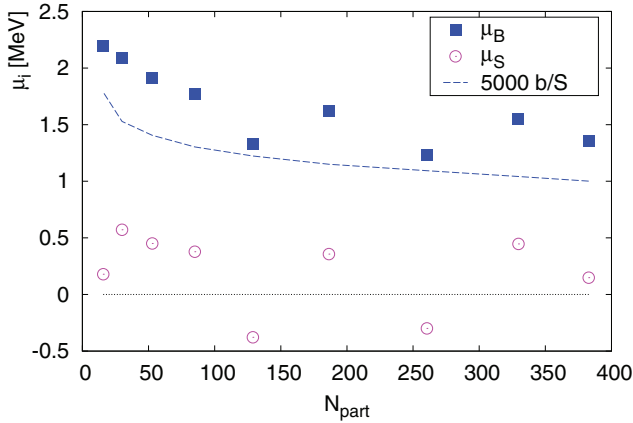


FIG. 10. (Color online) Scatter plot of fitted chemical potentials. The dashed line shows net baryon number over entropy b/S scaled with 5000.

for the most central collisions at LHC2760 there is some indication that $\mu_B \simeq 1.5$ MeV. The dashed line in Fig. 10 indicates the resultant baryon per entropy, b/S , scaled with 5000, these values are also seen in Table III. This is a first estimate of this important result needed for comparison with the conditions prevailing in the big-bang early universe, where $b/S \simeq 3.3 \times 10^{-11}$ [38].

B. p/π ratio and chemical (non-)equilibrium

The key difference between the three SHM approaches are the values of $\gamma_{q,s}$, as seen in Fig. 9(c). In Sec. II A, we argued that the baryon-to-meson ratio, e.g., p/π , is directly proportional to γ_q and this can be used to distinguish between the three SHM approaches. This ratio is a big problem for the equilibrium SHM [6]. We wish now to quantify this result within our approach and to show that, within the chemical nonequilibrium SHM, the problem is solved.

For this purpose, we redo all fits but making this ratio more explicit in the data analysis. Specifically, first we evaluate the p/π ratio based on the yields of p and π seen in Table I

$$\frac{p}{\pi} \equiv \frac{p + \bar{p}}{\pi^- + \pi^+}. \quad (7)$$

We estimate the error of the p/π ratio by adopting the relative error of p/π from [6], that is, 6.5%. We include this new data point, the p/π ratio, in the fit. Note that this increases the relative importance of p and π compared to the other particles included in the fit. Open symbols in Fig. 11(a) depict the data and solid symbols show the resulting output values obtained when we refit with enlarged data set that includes the p/π ratio. There is a minimal change in statistical parameters and physical properties of the fireball which we do not restate. In Fig. 11(b), we show χ^2_{total} .

Even with the increased importance of p/π , the chemical nonequilibrium SHM works very well. However, SHM with fixed $\gamma_q = 1$ have increased difficulties describing this ratio; that is, there is systematic 1.5–2 s.d. difference of the fit result and data and the value of χ^2_{total} is large. When compared to the χ^2_{total} obtained without the added p/π in Fig. 2, the

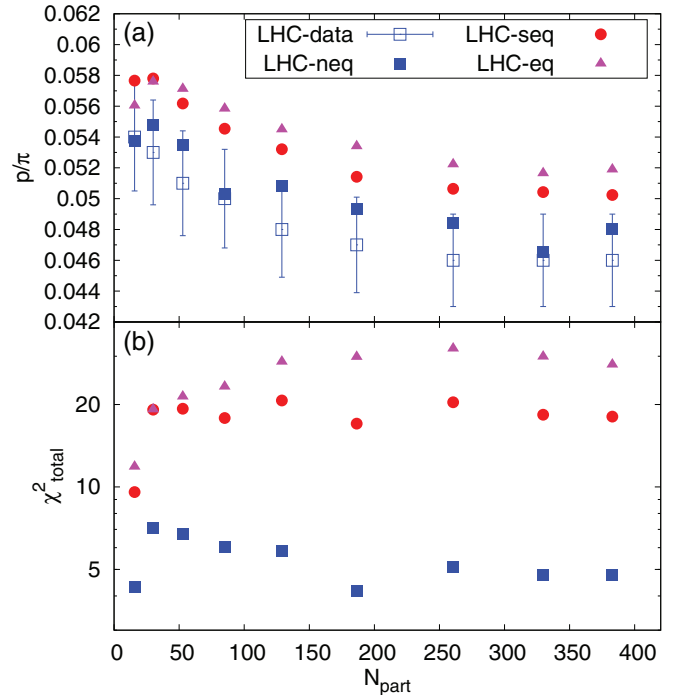


FIG. 11. (Color online) (a) Data and SHM description of p/π ratio fitted together with all other data within the three SHM approaches as a function of centrality. (b) Resulting χ^2_{total} for the three variants. See Sec. III B for details.

nonequilibrium variant shows nearly the same values of χ^2_{total} for all centralities, the p/π ratio is a natural outcome of the nonequilibrium approach. However, SHM approaches with $\gamma_q = 1$ show additional systematic increase in χ^2 by a factor of ~ 1.3 – 1.5 for all centralities. This means that the p/π data are in conflict with the hypothesis $\gamma_q = 1$. This demonstrates that the hypothesis of chemical equilibrium of light quarks is incompatible with the baryon-to-meson ratio at LHC2760 and $\gamma_q \simeq 1.6$ is needed to describe the LHC data. This finding is in agreement with the RHIC200 data [39], where the importance of the p/π ratio was noted.

To compare p/π ratio with our predictions, recall that the picture of universal hadronization condition with universal hadronization pressure $P = 82 \pm 5$ MeV has been advanced by our group [11,35,40]. For this favored hadronization condition, the p/π ratio is predicted in Table II of Ref. [41] to be $p/\pi = 0.047 \pm 0.002$, which agrees practically exactly with the experimental result shown in Fig. 11(a). The ALICE collaboration [30] considers and discusses the mechanism of chemical equilibrium hadron production followed by posthadronization interactions [42–46], specifically proton-antiproton annihilation, to justify the small p/π ratio, as compared to the result of equilibrium SHM alone. However, the annihilation mechanism was proposed based on preliminary data available in a single centrality bin 0%–20%, whereas our work includes more recent and centrality-dependent experimental results [30], allowing a far more conclusive study of the annihilation model.

Aside from $p\bar{p}$ annihilation, there are $p\bar{p}$ formation events. The significantly larger abundance (and therefore also density)

of heavy mesons compared to nucleons (see Table II) implies that mesons can be an effective source of nucleon pairs in reactions such as $p + \bar{p} \longleftrightarrow \rho + \omega$ and many other relevant reactions; see Table II in Ref. [47]. ALICE collaboration notes, that p/π ratio modification after annihilation should disappear in most peripheral collisions owing to smaller volume. We now quantify this effect showing how this fade-out of the annihilation effect would work as a function of centrality. We show that, given the constant p/π ratio in a wide range of centralities [Fig. 11(a)], the effect of posthadronization change of p/π ratio must be negligible.

To establish the centrality dependence of posthadronization nucleon yield changing reactions, we evaluate the total number of $p\bar{p}$ annihilation events. This number is obtained by integrating annihilation rate over history of the posthadronization matter expansion,

$$N_{\text{annih}} = \int dt N_{\bar{p}}(t) \rho_p(t) \sigma_{\text{annih}} v, \quad (8)$$

where v is the relative velocity of \bar{p} and p . The three-dimensional dilution of the density can be modeled as

$$\rho_p(t) = \frac{\rho_p^h}{(1 + \langle v_{\text{flow}} \rangle t / \langle L \rangle)^3}, \quad \langle L \rangle \simeq [(dV/dy)/(4\pi/3)]^{1/3}, \quad (9)$$

where $\langle L \rangle$ is the magnitude of the fireball size, and $\langle v_{\text{flow}} \rangle \simeq 0.6-1c$ is the velocity of the fireball expansion, in both cases averaged over the fireball complex three-dimensional geometry.

The initial density at time of hadronization is obtained from our hadronization study:

$$\rho_p(t_h) \equiv \rho_p^h \simeq \rho_p^h \equiv \frac{dN_p/dy}{dV/dy}. \quad (10)$$

In a wide range of low relative energies, which are relevant here, the event cross section is [48]

$$\sigma_{\text{event}} \equiv \sigma_{\text{annih}} v/c \simeq 46 \text{ mb}. \quad (11)$$

Neglecting the depletion of nucleons [i.e., $N_{\bar{p}}(t) \simeq N_{\bar{p}}^h$], we find, combining Eq. (8) with Eq. (9), the ratio of annihilated (anti)protons to their total yield $N_{\text{annih}}/N_{\bar{p}}^h$ and proton mean path before it annihilates L_{event} :

$$\frac{N_{\text{annih}}}{N_{\bar{p}}^h} = \frac{\langle L \rangle}{2\langle v_{\text{flow}}/c \rangle L_{\text{event}}}, \quad L_{\text{event}} = \frac{1}{\sigma_{\text{event}} \rho_p^h}. \quad (12)$$

The upper three lines, in Fig. 12, show L_{event} for the three models of hadronization (equilibrium, semiequilibrium, and nonequilibrium) as a function of centrality. The colored band in Fig. 12 represents the error originating from the freeze-out temperature T uncertainty (see Fig. 9). Note that the nonequilibrium model has much smaller parameter errors, so L_{event} is defined more precisely. The event reaction cross section for annihilation is well measured and nearly constant, thus it does not introduce any additional uncertainty to L_{event} . The bottom three lines, in Fig. 12 (semiequilibrium and equilibrium lines overlap, because dV/dy is very similar in these two cases), show how the size $\langle L \rangle$ of the system changes as a function of centrality. Especially for peripheral

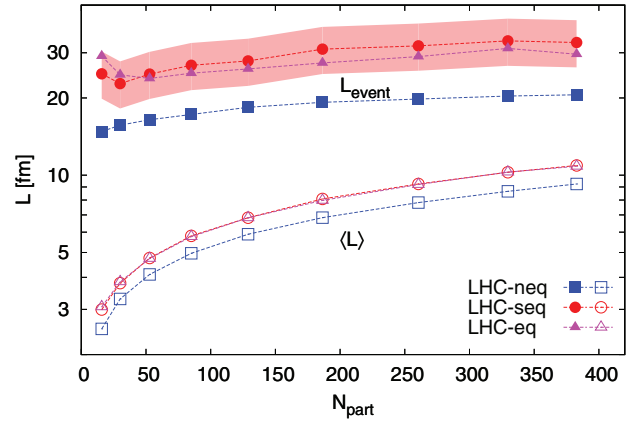


FIG. 12. (Color online) Solid symbols, antiproton annihilation event path L_{event} for the three SHM models as a function of centrality; open symbols, fireball size scale $\langle L \rangle$. The shaded error band represents error margin originating from the uncertainty of T (semi)equilibrium SHM. For readability, we omit much smaller error bands for nonequilibrium SHM.

collisions, we see that $\langle L \rangle \ll L_{\text{event}}$. The ratio of both length scales provides a measure of the fraction of protons that can be annihilated.

As seen in Fig. 12, from central to semiperipheral ($N_{\text{part}} \simeq 85$) collisions, the ratio of both lengths nearly doubles. This means that the annihilation fraction drops in semiperipheral collisions to about half of the most central value. However, the measured ratio p/π is nearly constant over this range, increasing from 0.046 ± 0.003 to 0.050 ± 0.003 . We interpret this as experimental evidence that the net effect of $p\bar{p}$ formation and annihilation is insignificant. Therefore, the annihilation of $p\bar{p}$ pairs cannot serve as the explanation of the disagreement between the equilibrium SHM and observed small value of p/π ratio.

Our estimate of the annihilation effect based on Eq. (12) and the result seen in Fig. 12 is consistent with the annihilation effect reported in Ref. [42], where detailed balance reactions forming $p\bar{p}$ were not considered. In this work, p/π rises to $p/\pi = 0.058$ already in the 20%–30% centrality bin ($N_{\text{part}} = 185$), which is more than 3 s.d. above experimental data [see Fig. 11(a)]. Another work, Ref. [44], addresses directly our scenario of describing the experimental p/π ratio and shows that with annihilation the required temperature would be $T = 165 \pm 5$ MeV, while without baryon annihilation a hadronization temperature of $T = 145 \pm 5$ MeV is required (initial yield from equilibrium SHM). Such models of posthadronization interactions also predict depletion of Ξ yield and enhancement of Ω yield [44–46], which leads to even greater discrepancy between at least one of the multistrange baryons and equilibrium SHM predictions, because these yields as obtained before annihilation are already, in general, below the experimental data [see Figs. 1(a) and 1(c)].

We do not see a scenario that would allow equilibrium SHM with hadronic afterburners to remain a viable model which can explain (a) the reduction of the p/π ratio from the equilibrium SHM value as a function of centrality and (b) the yields of the multistrange baryons at the same time. However,

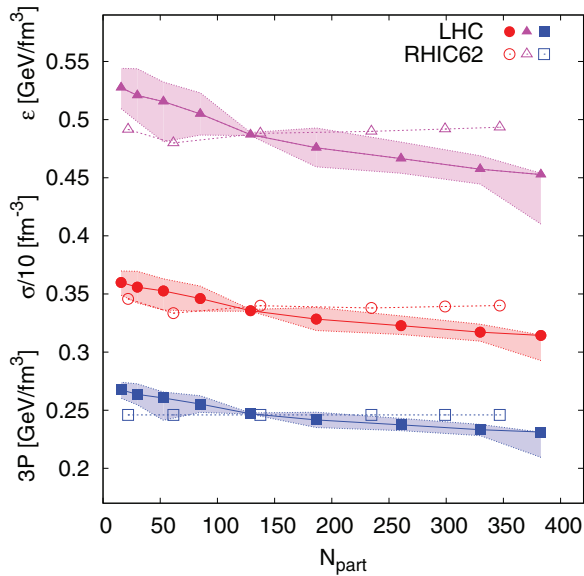


FIG. 13. (Color online) Bulk properties of the fireball as a function of centrality. From top to bottom, energy density ϵ (purple triangles), the entropy density σ (red circles), scaled down by factor 10, and the hadronization pressure $3P$ (blue squares); LHC2760 values are shown with solid symbols, RHIC62 values are shown with open symbols for comparison. Shaded areas show our estimate of systematic error arising from the uncertainty of γ_s .

the experimental value of p/π ratio was predicted [41]. The experimental result, the almost centrality-independent p/π ratio seen in Fig. 11 (note that the scale is greatly enhanced) is now successfully fitted within nonequilibrium SHM in this work without any modifications to the model or essential change in model parameter values.

C. Fireball bulk properties

To obtain the bulk physical properties of the source of hadronic particles, we use exactly the same set of particles and the same assumptions about their properties that we employed in the fit procedure. Therefore, the physical properties we determine are consistent with the particle yields that originated our fit. In other words, we sum the energy, entropy, etc., carried away by the observed particles, adding to this observed yield the contributions owing to unobserved particles used in the SHM fit.

The bulk physical properties of the hadronizing fireball, that is, energy, pressure, entropy, and strangeness per entropy content, are shown in the bottom part of Table III and in Fig. 13, where shaded domains show our error estimate. Solid symbols are results of the fit; lines guide the eye. In our SHAREV2 fit with MINOS minimization, the largest uncertainty seen in Table III is the γ_s and dV/dy error (see Fig. 9); other statistical bulk properties have relatively insignificant errors. As can be seen in Table III, multidimensional fits to data can result in nearly all of the fit error accumulating in the uncertainty of two or even just one parameter. In our fits, we see that the dominant uncertainty is in the volume normalization.

When error is found in a few if not only one parameter, we checked for uncertainty arising within an experimental data stability test. We test how a fit is modified when a small subset of experimental data points is altered arbitrarily but within error. We find that fits comprising input data with such arbitrary modification have, in general, larger errors distributed among all parameters. The convergence of the intensive parameters (e.g., T) in our initial fit suggests only a very small statistical error inherent to the data, while the extensive parameters (e.g., V) show a large error common to particle yield normalization. In this situation, predicted ratios of hadron species should be more precise than their individual errors suggest. This is attributable to the experimental normalization of particle yields being, as this study indicates, strongly correlated. The presence of not vanishingly small error in γ_s could be a signal of additional source of strange hadrons, for example, charm hadron decays.

All fit errors propagate into the properties seen in Fig. 13. Because in Fig. 9 we consider densities, the error in volume does not affect these values. Therefore, by recomputing the properties of the fireball shifting along the value of γ_s within 1 s.d., we obtain a good error evaluation in the measurement of the bulk physical properties shown in Fig. 13. The point that stands out with very small error is at $N_{\text{part}} = 130$. This anomaly is attributable to accidental appearance of a sharp minimum in the highly nontrivial seven-dimensional parameter space.

We are interested in studying the bulk properties of the source of hadrons to test the hypothesis that a QGP fireball was the source of particles observed. For this to be true, we must find appropriate magnitude of bulk properties consistent with lattice results, and at the same time, a variation as a function of centrality that makes good sense. We observe in Fig. 13 a smooth and slow decrease of energy density ϵ (top), entropy density σ (middle), and hadronization particle pressure P (bottom) as a function of centrality. This slow systematic decrease of all three quantities is noted, in particular, comparing to RHIC62 (open symbols), where the properties seem to vary less. This maybe interpreted as an effect of volume expansion at LHC, leading to larger supercooling for larger systems.

The local thermal energy density of the bulk is the source of all particles excluding the expansion flow kinetic energy. The value we find is $\epsilon \simeq 0.50 \pm 0.05$ GeV/fm³ in the entire centrality range. Nearly the same value is found within the chemical nonequilibrium approach for RHIC62 [12] and RHIC200 [10]. We note that ϵ assumes the smallest value for the most central collisions; see Table III and Fig. 13. The hadronization pressure P and entropy density σ are also decreasing for more central collisions, which is consistent with our reaction picture of expanding and supercooling fireball; the larger system in central collisions exhibits more supercooling reflected by a decrease of hadronization temperature and the above-mentioned behavior of bulk properties. The error band is (as for ϵ) based on γ_s uncertainty.

In the last row of Table III, we show that entropy yield at LHC2760 is more than 3 times greater than obtained at RHIC62. The entropy yield dS/dy as a function of participant number is shown in Fig. 14, and the notable feature is that the power-law parametrization displays a nearly linear dependence at RHIC62 while at LHC2760 a strong additional

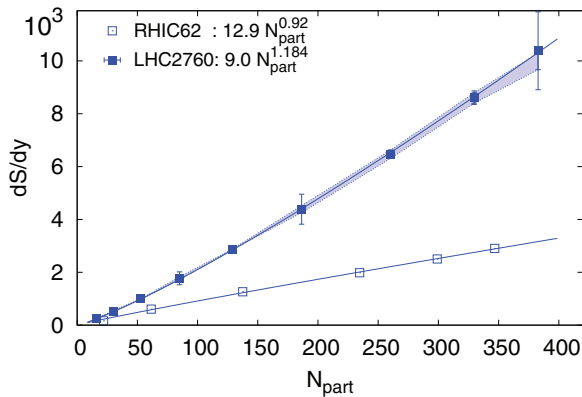


FIG. 14. (Color online) Entropy yield dS/dy at LHC2760 and at RHIC62 as a function of centrality showing power-law fit parameters in the legend. The colored band represents uncertainty based on γ_s fit uncertainty. Error bars arise from error in the volume dV/dy .

entropy yield, associated with the faster-than-linear increase, is seen: $dS/dy \propto N_{\text{part}}^{1.184}$. Most of the entropy is produced in an initial-state mechanism which remains to be understood and our finding of the nonlinear entropy growth with N_{part} adds to the entropy production riddle an important observational result.

However, at LHC2760, one expects a component in the entropy count arising from the inclusion of the decay products of heavy charmed hadrons in the hadron yield. This entropy component is different from entropy produced in initial reactions; this is the entropy arising from hard parton collision production of charm and posthadronization decay of charmed hadrons. It is unlikely that the nonlinearity of the entropy yield is attributable to this phenomenon, as one can easily see that the required charm yield would be very large. We will return, in the near future, to this question. The uncertainty of entropy depicted in Fig. 14 as a shaded band is based alone on γ_s variation, as was obtained for other physical properties in Fig. 13. A further error owing to variance in dV/dy is shown as a separate error bar. Where it is invisible for the LHC2760, it is hidden in symbol size.

We turn now to study strangeness per entropy $s/S \equiv (ds/dy)/(dS/dy)$ in the source fireball. We are interested in this quantity because both entropy and strangeness yields are preserved in the hadronization process. Therefore, by measuring s/S , we measure the ratio of strange quark abundance to total quark and gluon abundance, which determines the source entropy, with a well-known proportionality factor. For the presently accepted small strange quark mass $m_s(\mu = 2 \text{ GeV}) = 95 \pm 5 \text{ MeV}$ [49], the predicted value shown in Fig. 5 of Ref. [50] is $s/S \simeq 0.0305 \pm 0.0005$. Finding this result in our LHC data analysis is necessary to maintain the claim that the source of hadrons is a rapidly disintegrating chemically equilibrated QGP fireball.

In Fig. 15(a), we show the strangeness per entropy s/S in the source fireball. The solid squares are for the LHC2760, and the open symbols are for RHIC62. We see that s/S saturates at $s/S \simeq 0.030$ at LHC2760, a value reached already for $N_{\text{part}} > 150$, thus for a smaller number of participating nucleons than we found at RHIC62 and which value remains constant up

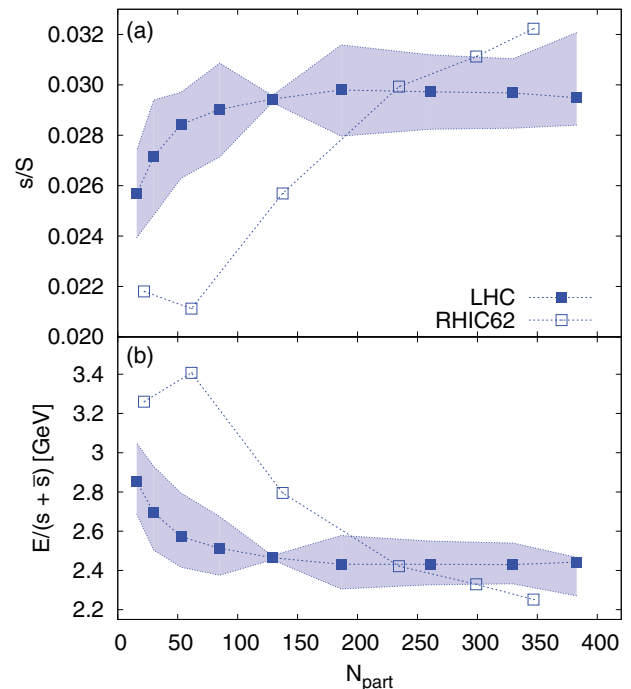


FIG. 15. (Color online) (a) Strangeness per entropy s/S content of the fireball at LHC2760 (solid squares) and at RHIC62 (open squares) as a function of centrality; (b) the thermal energy cost to make a strange-antistrange quark pair. Colored bands represent uncertainty based on γ_s uncertainty.

to the maximum available N_{part} . This agrees with equilibrated QGP hypothesis and suggests that the source of hadrons was under the same conditions for a wide range of centrality.

This constant s/S value as a function of centrality can be interpreted as an evidence of chemical equilibrium for a QGP source: The strangeness yield normalized to all quark and gluon yield inherent in S can be constant only if dynamical processes find a chemical balance for the differently sized fireballs. The value $s/S = 0.03$ is in excellent quantitative agreement with microscopic model of strangeness production and equilibration in QGP [50,51], adopting the latest strange quark mass value. The high QGP strangeness yield oversupplies in hadronization the hadron phase space, resulting in $\gamma_s \simeq 2$ seen in Fig. 9. Considering the RHIC results shown in Fig. 15(a), we see a slightly higher s/S saturation limit for most central collisions, though the difference is within the RHIC error band (not shown). It is possible that the s/S LHC2760 result is 5%–10% diluted owing to inadvertent inclusion in the entropy count of the charm-decay hadrons. It is also of interest to note that at RHIC62, s/S increases monotonically (discounting the low confidence level most peripheral point) with increasing N_{part} , suggesting that the QGP source reaches chemical equilibrium only for most central collisions. At LHC2760 there is such increase for much smaller size fireball corresponding to the smaller collision centrality $N_{\text{part}} < 150$.

In Fig. 15(b), we show the thermal energy cost to make a strange quark-antiquark pair. At LHC2760, the energy cost to make a strange pair is practically constant for the wide range of midcentral to central collisions, which confirms that

strangeness in the QGP fireball is in chemical equilibrium at the time of hadronization. The slight increase of the thermal energy cost for small centralities corresponds to the lower yield of strangeness seen in Fig. 15(a). At RHIC62, we see monotonically improving energy efficiency converging to a value slightly below our new LHC2760 result, but well within the error bar at RHIC62 (not shown). The rise of energy cost for smaller systems relates to the fact that a larger and notable fraction of strangeness was produced in first hard-collision processes during the initial stages of the collision which for RHIC62 and LHC2760 results in the higher energy needed to produce one strange-antistrange pair.

D. Connection to lattice results and related considerations

Elaborate lattice-QCD numerical computations of QGP-hadron transition regime are available today [24,25] and are comprehensively reviewed in Ref. [26]: the HotQCD collaboration [25] converged for 2 + 1 flavors towards $T_c = 154 \pm 9$ MeV. The question of how low the value of T_c can be remains in current intense discussion, as the latest work of Wuppertal–Budapest collaboration [27] suggests a low $T_c \simeq 145$ MeV. For an expanding QGP with supercooling, this can lead to hadronization below $T_c \simeq 145$ MeV and near $T = 140$ MeV. This is indeed the range of values of T that we find in our chemical nonequilibrium SHM analysis.

A comparison of lattice results with freeze-out conditions is shown in Fig. 16. The two bands near to the temperature axis display the lattice critical temperature in the range $T_c = 154 \pm 9$ MeV [25] (red online) and $T_c = 147 \pm 5$ MeV [27] (green online). The symbols show the results of hadronization analysis in the T - μ_B plane. We selected here the results for the most central collisions and the heaviest nuclei. The solid (blue) circles are SHARE chemical nonequilibrium results obtained by our group, with result presented in this paper included in the LHC domain and RHIC and SPS results seen, e.g.,

in Refs. [11,40,52]. The LHC2760 freeze-out temperature is in our case clearly below the lattice critical temperature T_c . As just discussed, this is expected for supercooling followed by sudden hadronization. We show also $\gamma_q = 1$ results of other groups: GSI [53,54], Florence [15,55,56], THERMUS [57], STAR [58], and ALICE [6]. These results show the chemical freeze-out temperature in numerous cases well above the lattice critical temperature T_c , which, in essence, means that these SHM calculations are incompatible with lattice calculations.

The two recent lattice results, shown in Fig. 16, challenge the chemical equilibrium hadronization [14] scenario widely used for the past decade, which produces a hadronization temperature above the lattice phase crossover results. Two complementary hypotheses were made in Ref. [14]: (1) there is chemical equilibrium in (2) a long-lived hadron gas phase. Both statements were assumptions without theoretical or experimental evidence “confirmed” by fits to data, which had, even with the large experimental errors, a rather large χ^2 and thus a negligible confidence level. Therefore, this model needed additional support. Lattice results showing $T_c = 173 \pm 8$ MeV were often introduced in support of equilibrium-SHM. Such a high T_c appears, for example, in Fig. 10 of Ref. [59], but reading the text, one sees that it applies to the mathematical case of two light quark flavors on discrete space-time. Allowing for strangeness flavor in QGP, the hadronization temperature must decrease. Therefore, already a decade ago $T_c = 154 \pm 8$ MeV was the best estimate for 2 + 1 flavors, leading to the consensus range $T_c = 163 \pm 15$ MeV before continuum limit. Present-day continuum value we estimate to be $T_c \simeq 150 \pm 7$ MeV combining the two results seen in Fig. 16.

An important requirement for the full chemical nonequilibrium hadronization approach is that in the hadronization process, quark flavor abundances emerge as produced at an earlier and independent stage of fireball evolution. Our analysis relies on hadronization being fast, not allowing a significant modification of the available quark abundances. These quark abundances at LHC in a wide range of centralities and in most central RHIC collisions are near to the QGP chemical equilibrium abundance. For the quark yields to remain largely unchanged during hadronization and after, it is necessary that the transformation from QGP to hadrons (hadronization) occurs suddenly and at a relatively low temperature, near the expected chemical freeze-out point, where particle abundances stop evolving. The two-pion correlation experimental results favor sudden hadronization, which has been seen in the results for a long time [21]. The sudden hadronization model was required for consistency with these results [22,23]. It is associated with chemical nonequilibrium SHM analysis of the data [7,8]. Today, with lattice QCD transition conditions reaching a low- T consensus, the only SHM approach that remains valid is the chemical nonequilibrium.

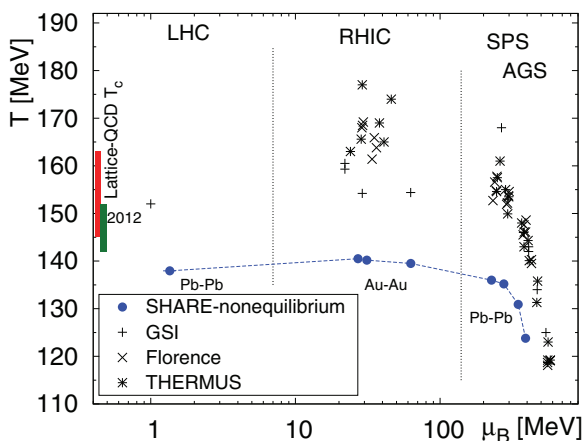


FIG. 16. (Color online) Phase diagram showing current lattice value of critical temperature T_c calculated by two groups [25,27] and results of this work, as well as our previous results (blue circles) [7,40,52] and results of other groups [6,15,53–58]. Solid circles refer to chemical nonequilibrium; all other symbols refer to fit results with chemical equilibrium of light quarks.

IV. DISCUSSION

A. What is new at LHC

The primary difference between RHIC62 and LHC2760 data is a 4-times-larger transverse volume dV/dy at

hadronization, as seen in Fig. 9(a). The increase of volume at LHC compared to RHIC, rather than a change of hadronization temperature, shows a common source of hadrons, a signature of QGP formation. The increased volume is in qualitative agreement with the two-pion correlation studies [60]. Given the nearly constant entropy density at hadronization, the growth of volume drives the total entropy yield, which is up to 3.2 times greater at LHC2760 than at RHIC62.

Other differences of LHC2760 compared to RHIC62 are

- (i) an order-of-magnitude-smaller baryochemical potential $\mu_B \simeq 1.5$ MeV (see Fig. 10);
- (ii) phase-space occupancy γ_q constant as a function of centrality;
- (iii) earlier saturation of γ_s as a function of centrality, and thus γ_s/γ_q ratio following the behavior of γ_s .

For comparison, at RHIC62, we have a fast increase of γ_s over the entire range of N_{part} , as is shown in Fig. 9(c). The LHC2760 result is interpreted to mean that the QGP fireball is rapidly chemically equilibrated already for small N_{part} , while at RHIC62, we must have a large value of N_{part} , that is a large volume, and thus large life span, to achieve full strangeness chemical equilibrium in the QGP fireball. The value $s/S = 0.03$ is in excellent qualitative agreement with microscopic model of strangeness production and equilibration in QGP and the associated predictions of the final-state yield [50,51].

As a comparison of our present work with our predictions [41] shows, the yield of strangeness is $\sim 20\%$ below our prior expectations. These were motivated by consideration of a very rapidly diluting QGP fireball, wherein the early strangeness QGP equilibrium is preserved and leads to overabundance, above QGP chemical equilibrium at time of hadronization. Such behavior was indicated given the RHIC results showing a steady rise; see Fig. 15(a) for RHIC62. Instead, we find a perfectly equilibrated QGP fireball: The observed value of $s/S \simeq 0.03$ is expected for a chemically equilibrated QGP fireball near hadronization condition. This equilibrium QGP saturated value $s/S = 0.03$ is observed for many centralities. Because to obtain our prediction we used $s/S = 0.037$, both the value of γ_s and yields of kaons are equally $\sim 20\%$ suppressed compared to expectation [41], as are other strange particles. How this is possible will be one of the riddles that future data and theoretical modeling will need to address. For us, this strangeness suppression compared to expectation is the most remarkable difference from RHIC data that we have found in this first LHC result analysis.

B. Centrality dependence

Considering the bulk properties of the fireball at hadronization, the most remarkable finding is that there is so little centrality dependence. This means that at LHC2760 the source of hadrons is a hot drop of energy that varies mainly in volume as we vary the collision geometry. This applies to energy density $\varepsilon \simeq 0.50 \pm 0.05$ GeV/fm³, hadronization pressure P , and entropy density σ in the entire centrality range; see Table III and Fig. 13. These bulk properties decrease monotonically and slowly and assume the smallest value for the most

central collisions, supporting the reaction picture of expanding and supercooling fireball; the larger system supercools a bit more. Recall that the error bands in Fig. 13 are based on γ_s uncertainty. The one clear centrality dependence of the fireball we find is the rapid rise and early appearance of the strangeness yield saturation seen in Fig. 15(a).

The chemical freeze-out temperature T decreases by about 3 MeV at all centralities compared to RHIC62; see middle panel in Fig. 9 (we do not consider here the most peripheral RHIC62 result, which has a small confidence level). We believe that this result is related to the need to expand and supercool further the initial energy and entropy rich LHC2760 fireball. The large expanding QGP matter pushes further out, supercooling more and yielding a further reduction in the sudden hadronization temperature. The freeze-out temperature T increases towards more peripheral collisions [see Fig. 9(b)], which can be explained by the disappearance of supercooling present for the most central and most energetic collision systems. Considering the behavior of both LHC2760 and RHIC62 for $N_{\text{part}} \rightarrow 0$, we obtain $T_{\text{had}} \rightarrow 145 \pm 4$ MeV, applicable to hadronization without supercooling. This value is in good agreement with the latest lattice result [27] for transformation temperature from QGP to hadrons.

The value of temperature and its behavior as a function of centrality and heavy-ion collision energy suggest that produced hadrons emerge directly from a sudden breakup of quark-gluon plasma. The hadron particle density at this low T is sufficiently low to limit the particle number changing reactions and render these insignificant. $T = 145\text{--}140$ MeV is at and below the expected QGP phase transition. The presence of chemical nonequilibrium at this low T means that hadrons did not evolve into this condition, but must have been produced directly from the deconfined phase. This is consistent with the two-pion correlation time parameter, which suggests that particles are produced at a scale which is sudden compared to the size of the system, as is expected for a supercooled QGP state undergoing, e.g., a filamenting breakup at $T \simeq 140$ MeV, and the result of such dynamics is qualitatively consistent with the features described here [21].

The second-to-last row in Table III shows the ratio of entropy at LHC2760 to RHIC62, $S_{\text{LHC}}/S_{\text{RHIC}}$, within the rapidity interval $-0.5 \leq y \leq 0.5$. The entropy enhancement factor increases monotonically with centrality, from ratio of 1.27 in the most peripheral bin to ratio 3.23 in the most central bin. This increase requires volume-dependent additional entropy production mechanisms, which are more effective for the more central, larger N_{part} , collisions. Such an increase can arise from hard-parton-collision-generated jets, which are better quenched in the larger volume of matter, and, in addition, in abundant charm production, which decays into hadrons and appears as additional hadron multiplicity, i.e., entropy. As long as the additional entropy is generated in early stages of the fireball evolution, this has little impact on SHM method of approach in study of hadronization. For example, the quenching of QCD jets feeds thermal degrees of freedom that can convert a part of its energy into strangeness. However, charm decay is different because it occurs after hadronization. Thus, it needs to be accounted for and/or proved irrelevant. It is possible that a charm-decay entropy-generating mechanism

may be the cause of the slight (5%) strangeness s over entropy S dilution at LHC2760 [see Fig. 15(a)].

C. What we learn about hadronization at LHC

The full chemical nonequilibrium is introduced by the way of the parameter $\gamma_q \neq 1$. This allows one to describe a situation in which a source of hadrons disintegrates faster than the time necessary to reequilibrate the yield of light quarks present. The two-pion correlation data provide experimental evidence that favors a rapid breakup of QGP with a short time of hadron production [21], and thus favors very fast, or sudden, hadronization [22,23]. There has been for more than a decade an animated discussion if the parameter γ_q is actually needed with arguments such as simplicity used to invalidate the full chemical nonequilibrium approach.

We have shown that *only* the chemical nonequilibrium SHM describes very well all available LHC2760 hadron production data obtained in a wide range of centralities obtained in the rapidity interval $-0.5 \leq 0 \leq 0.5$, and the outcome is consistent with lattice QCD results. We successfully fit the data with $\chi^2/\text{ndf} < 1$ for all centrality bins, and show a smooth systematic behavior as a function of centrality of both the statistical SHM parameters (see Fig. 9) and bulk physical properties (see Fig. 13) that allow a simple and consistent interpretation. SHM is validated at LHC2760 as it describes precisely yields of different particles in a wide range of collision centrality and which span over more than 5 orders of magnitude; see Fig. 6.

We have shown that it is impossible to fit the ratio $p/\pi = 0.046 \pm 0.003$ [5,6] together with the other data, when choosing a SHM with $\gamma_q = 1$. However, $p/\pi \simeq 0.05$ is a natural outcome of our chemical nonequilibrium fit where $\gamma_q \simeq 1.6$. This result was predicted [41]: Within the chemical nonequilibrium SHM, $p/\pi|_{\text{prediction}} = 0.047 \pm 0.002$ for $P = 82 \pm 5 \text{ MeV/fm}^3$ is in agreement with experimental result we discuss here, for most central collisions $p/\pi|_{\text{ALICE}} = 0.046 \pm 0.003$.

We have discussed, in Sec. III B, the possibility of the p/π ratio evolving after hadronization and found this scenario to be highly unlikely considering that experimental ratio p/π does not vary in a wide centrality domain. Therefore, the fact that chemical equilibrium SHM variant overpredicts p/π and produces a poor χ^2_{total} , see Fig. 11(b), demonstrates that the chemical equilibrium SHM approach (with or without posthadronization interactions) does not work at LHC2760. Further evidence for the chemical nonequilibrium SHM comes from the universality of hadronization at LHC2760 and at RHIC; see Sec. III C and Ref. [35].

D. Predicting experimental results

Our prediction of hadron yields [41] required as input the charge particle multiplicity dN_{ch}/dy , which normalizes the reaction volume dV/dy . Further, we assumed strangeness per entropy content s/S , and the nearly universal hadronization pressure with preferred value $P = 82 \pm 5 \text{ MeV/fm}^3$. This is accompanied by the strangeness conservation constraint $\langle s - \bar{s} \rangle = 0$ and the projectile-target charge to baryon ratio $Q/B = 0.4$ and, as baryochemical potential cannot yet be

fully defined, an approximate value $\mathcal{O}(1)$ MeV. Using this input with a 5% error, we obtain the most compatible values of dV/dy , T , γ_q , γ_s and chemical potentials, and we can evaluate the particle yields along with fireball properties.

We have redone the predictions for $\sqrt{s_{NN}} = 2.76 \text{ TeV}$ case with the tested and released SHAREV2.2 code and find that the prerelease SHARE predictions in Ref. [41] were made for $dN_{\text{ch}}/dy = 2150$ and not for $dN_{\text{ch}}/dy = 1800$. Therefore, all absolute hadron yields stated in Ref. [41] are normalized to be $\sim 20\%$ too large, in addition to the strangeness overcount originating in the assumption $s/S = 0.037 > 0.030$. The ratios of hadrons with the same strangeness content were correctly predicted.

Applying our prediction method using the updated strangeness value of $s/S = 0.030$ and a more precise hadronization pressure estimate $P \simeq 77 \pm 4 \text{ MeV/fm}^3$ results, for $\sqrt{s_{NN}} = 2.76 \text{ TeV}$, in the accurate prediction of all hadron particle yields, statistical parameters, and fireball bulk properties, without using as input any individual hadron yield. This validates our approach [41], which can be applied to the forthcoming Pb-Pb collisions at $\sqrt{s_{NN}} = 5.5 \text{ TeV}$ or in the RHIC beam energy scan. Noting that the multiplicity of produced hadrons is synonymous with entropy of the fireball, this result means that all hadron yields can be predicted within the framework of chemical nonequilibrium SHM using as input the properties of the bulk matter in the fireball.

E. Conclusions and outlook

We have shown that the nonequilibrium SHM model in the LHC reaction energy range is yielding a very attractive data fit. We have argued that nonequilibrium SHM is today favored by the lattice results, because we must have $T < T_c$, and the lattice is moving lower in T_c ; see $T_c = 147 \pm 5 \text{ MeV}$ [27]. Only the nonequilibrium SHM range $T < 145 \text{ MeV}$ remains convincingly compatible, considering the dynamics of the fireball expansion $\Delta T \equiv T_c - T$ is of magnitude where we would like it for supercooling. Moreover, the chemical nonequilibrium SHM is favored by offering simplicity, as it needs no afterburners. Occam's razor argument (*lex parsimoniae*) can be used to conclude that nonequilibrium SHM is a valid precise description of multihadron production.

The good fit within the realm of nonequilibrium SHM of all observed particles allows us to predict with some confidence the yields of yet-unmeasured hadrons within the chemical nonequilibrium SHM scheme, which are seen in Table II. The question is how stable these yields are when data basis of the fit increases to include new measurement. A small SHM parameter change should be expected also when we refine the theoretical model by adding features, such as inclusion of hadrons from perturbative QCD jets and/or charm hadron decay contribution to hadron yields. We believe that predictions for the primary "stable" hadrons such as η are accurate. However, even the minor changes in SHM parameters can have a relatively large effect, especially for antimatter clusters shown in the bottom part of Table II: In the anti- α , we have 12 antiquarks, and a few % error in understanding their primordial yield is raised to 12th power.

It is quite remarkable that despite a change by a factor of 45 in reaction energy, we find for all centralities at both LHC2760 and RHIC62, that the energy density of hadronizing matter is 0.50 ± 0.05 GeV/fm³, as is seen in Fig. 13. In fact, the present-day data favor a systematic decrease of hadronization pressure P from peripheral towards central collisions as compared to earlier RHIC62 [12], RHIC200 [10] and our preliminary LHC analysis with limited data set [35]. It is possible that the more dynamical expansion of the LHC2760 fireball and deeper supercooling of the fireball are the cause.

We checked that assuming universal hadronization pressure, we could obtain a very good fit to particle data for all centrality LHC2760 data bins. This means that if and when more hadron yield data are available, the decrease in bulk properties with centrality seen in Fig. 13 could easily disappear. Therefore, the presence of a constant critical hadronization pressure [40] could extend from SPS to LHC. We are investigating this hypothesis, as well as the possibility that another quantity governs universality of hadronization. We hope to return to the matter as soon as we have understood better the final-state contributions to hadron yields from charmed hadron decays.

We have shown that the precise hadron yields measured by the ALICE collaboration at LHC2760 have offered a vast new opportunity to explore the properties of the QGP fireball and to understand the dynamics of its evolution and matter production. We are able to quantify the key physical properties at this early stage. With more data becoming available, we expect a significant refinement and improved understanding of both the QGP fireball and mechanisms of matter creation out of the deconfined QGP phase.

F. Update

We have verified that the new results [61,62] on strange hadron multiplicities which became available at the beginning

of the SQM2013 meeting at the end of July 2013 are fully compatible: The K_S , Ω , and Ξ are in remarkable agreement with our here-presented evaluations and Λ yield is as much off as the preliminary Λ/π ratio we fitted (see Fig. 7); that is, the theoretical Λ yield is in general about 1.2 s.d. smaller compared to the final experimental Λ yield. Here we note that the presented fits are carried out without taking into account charmed particle decay products, which, beyond the generally enhanced overall hadron multiplicity, produce a non-negligible number of additional strange baryons.

ACKNOWLEDGMENTS

This work has been supported by a grant from the US Department of Energy, Grant No. DE-FG02-04ER41318; Laboratoire de Physique Théorique et Hautes Energies, LPTHE, at University Paris 6 is supported by CNRS as Unité Mixte de Recherche, UMR7589. J.R. thanks CERN-PH-TH for the hospitality while most of this work was carried out. J.R. thanks members of ALICE collaboration, in particular Karel Safarik, Boris Hippolyte, and Federico Antinori, for many conversations and clarifications.

APPENDIX: DATA REBINNING

1. Rebinning multistrange hadron yields

Because there is no literature stating explicitly the yields of Ξ and Ω in Pb-Pb collisions, we proceed to obtain these results by unfolding the preliminary enhancement data. We combine the yield of Ξ and Ω produced in p - p collisions at 7 TeV [34] stated in Table IV and labeled “ pp ” in the third column therein, with the “preliminary” enhancement E relative to p - p and normalized to a pair of participating nucleons shown in Ref. [31] and which we also show in the fifth column of Table IV. We generate the first data point for the centrality

TABLE IV. Enhancement of multistrange baryon yields per participant pair relative to p - p collisions, p - p yields, and calculated yields in Pb-Pb, which we use as input to our interpolation as a function of N_{part} .

Particle	Ref.	Centrality	$\langle N_{\text{part}} \rangle$	p - p data $(dN/dy)_{pp}$ and enhancement E	$(dN/dy)_{\text{PbPb}} = E 0.8 (dN/dy)_{pp} (\langle N_{\text{part}} \rangle / 2)$	
Ξ^-	[34]	p - p	2	$(8.0 \pm 0.7) \times 10^{-3}$		
	[32]	60%–90%	17.6	$E = 1.58 \pm 0.18$	0.090 ± 0.010	
		40%–60%	68.8	$E = 2.48 \pm 0.26$	0.55 ± 0.06	
		20%–40%	157	$E = 2.95 \pm 0.32$	1.51 ± 0.17	
		0%–20%	308	$E = 3.08 \pm 0.33$	3.08 ± 0.33	
Ξ^+	[34]	p - p	2	$(7.8 \pm 0.7) \times 10^{-3}$		
	[32]	60%–90%	17.6	$E = 1.57 \pm 0.19$	0.087 ± 0.011	
		40%–60%	68.8	$E = 2.56 \pm 0.26$	0.56 ± 0.06	
		20%–40%	157	$E = 3.20 \pm 0.35$	1.59 ± 0.17	
		0%–20%	308	$E = 3.00 \pm 0.32$	2.91 ± 0.32	
Ω^-	[34]	p - p	2	$(0.67 \pm 0.08) \times 10^{-3}$		
		p - p	2	$(0.68 \pm 0.08) \times 10^{-3}$	Ω^-	$\bar{\Omega}^+$
$\frac{(\Omega^- + \bar{\Omega}^+)}{2}$	[32]	60%–90%	17.6	$E = 2.56 \pm 0.53$	0.012 ± 0.003	0.012 ± 0.003
		40%–60%	68.8	$E = 4.57 \pm 0.79$	0.08 ± 0.02	0.08 ± 0.02
		20%–40%	157	$E = 5.23 \pm 0.95$	0.22 ± 0.05	0.21 ± 0.04
		0%–20%	308	$E = 6.97 \pm 1.27$	0.57 ± 0.12	0.56 ± 0.12

bin 0%–20% by averaging the number of participants in the centrality bins from 0% to 20% shown in Table 1 of Ref. [29]. We reduce the yields of both Ξ and Ω by a constant factor of 0.8 to compensate for the difference in collision energy $\sqrt{s} = 7$ TeV in p - p collisions and $\sqrt{s_{NN}} = 2.76$ TeV in Pb-Pb. We obtained the magnitude of this energy correction factor by comparing with the actual yield for the 0%–20% centrality bin given in Ref. [28]. To disentangle the combined yield of $\Omega + \bar{\Omega}$, we use the separated Ω and $\bar{\Omega}$ yields from p - p collisions [34]; see Table IV.

We use the relative errors of the enhancements to estimate the errors of the multistrange baryon yields, that is $\sim 11\%$ for Ξ and $\sim 20\%$ for Ω . Our adopted Ω error is larger by $\sim 3\%$ than the error of its yield in the 0%–20% centrality bin [28]. We adopted this slightly increased error to account for a procedure which leads us to estimate the yield of Ω , $\bar{\Omega}$ based in part on $\Omega + \bar{\Omega}$ yield. The mathematical operations leading to the yields, the yields, and widths we use are stated in self-explanatory fashion in Table IV.

To account for the different centrality bins for multistrange baryons as compared to π , K , p , and ϕ/K , we express the centrality bins in terms of average number of participants according to [29] and then interpolate every particle yield dN/dy available as a function of N_{part} with a power law,

$$\frac{dN(N_{\text{part}})}{dy} = a N_{\text{part}}^b + c, \quad (\text{A1})$$

where a , b , and c are free parameters. The form of the function has no immediate physical motivation; it serves well the purpose of unifying the data across incompatible centrality bins. This method enables us to evaluate the invariant yields for any given N_{part} , i.e., arbitrary centrality, and thus enables us to include the multistrange baryon yields in this analysis. Interpolation parameters together with χ^2 of each particle interpolation are summarized in Table V. For completeness and potential future use, we present also the parametrization of π^\pm , K^\pm , and p^\pm which do not require rebinning. Small values of χ^2/ndf show that our description is accurate in the given interval of N_{part} . Interpolation curves are depicted with dashed lines in Fig. 6 for particle yields.

TABLE V. Interpolation parameters of particle yields as defined in Eq. (A1).

Particle	a	b	c	χ^2/ndf
π^+	0.725	1.160	-0.890	0.30/7
π^-	0.724	1.160	-0.864	0.22/7
K^+	0.0935	1.187	-0.174	0.07/7
K^-	0.0927	1.188	-0.158	0.06/7
p	0.0432	1.116	-0.047	0.32/7
\bar{p}	0.0502	1.089	-0.088	0.26/7
Ξ^-	0.005 52	1.108	-0.043	0.12/1
$\bar{\Xi}^+$	0.007 62	1.049	-0.067	0.70/1
Ω^-	0.000 286	1.324	-0.0006	0.40/1
$\bar{\Omega}^+$	0.000 309	1.308	-0.0011	0.21/1
K^{*0}/K^-	See text for details			0.032/1
Λ/π	See text for details			0.0054/1

TABLE VI. Experimentally measured ratios used as input to our interpolation as a function of N_{part} .

Ratio	Ref.	Centrality	$\langle N_{\text{part}} \rangle$	Experimental ratio
K^{*0}/K^-	[31]	60%–80%	22.6	0.333 ± 0.084
		40%–60%	68.8	0.285 ± 0.061
		20%–40%	157	0.245 ± 0.066
		0%–20%	308	0.194 ± 0.051
$\frac{2\Lambda}{(\pi^- + \pi^+)}$	[31]	60%–80%	22.6	0.0355 ± 0.0041
		40%–60%	68.8	0.0371 ± 0.0042
		20%–40%	157	0.0365 ± 0.0042
		10%–20%	261	0.0355 ± 0.0041
		0%–10%	357	0.0336 ± 0.0040

2. Rebinning K^{*0}/K^- , Λ/π hadron ratios

We include particle ratios K^{*0}/K^- , ϕ/K^- , and $\Lambda/\pi \equiv 2\Lambda/(\pi^- + \pi^+)$ [31]. This adds Λ , K^{*0} , and ϕ into our data set. Because in some ratios certain systematic uncertainties of individual yields cancel out, introduction of ratios is reducing the overall error of the global fit. The ratio ϕ/K has an experimental data point in each centrality bin we analyze, removing the need for interpolation or rebinning. Thus, the following addresses only K^{*0}/K^- and Λ/π .

There are four (five) data points for K^*/K (Λ/π), which we present in Table VI. We describe K^*/K dependence on N_{part} with a power law,

$$\frac{K^*}{K} = f(N_{\text{part}}) = 16.23(N_{\text{part}}^{-0.0034} - 1) + 0.512, \quad (\text{A2})$$

with total $\chi^2/\text{ndf} = 0.032/1$. Systematic behavior of Λ/π as a function of centrality is qualitatively different from K^*/K (see Fig. 7); a power law is not sufficient to properly describe the data. We use a sum of two power laws in the form

$$\frac{\Lambda}{\pi} = f(N_{\text{part}}) = -6.79 \times 10^{-5} N_{\text{part}}^{0.848} - 2 N_{\text{part}}^{-0.00135} + 2.03, \quad (\text{A3})$$

with $\chi^2/\text{ndf} = 0.0054/1$. In these two cases, the form of the ratio functions has no immediate physical meaning; it is invented to provide an accurate empirical description; note that the bottom of the Table V presents the fit quality of these two ratios.

Interpolation curves are depicted with dashed lines, in Fig. 7, for K^*/K and Λ/π ratios. To assign an error to the interpolated data points, we take the average nearby experimental error for the given particle yield or ratio. However, by extrapolating the K^*/K ratio to $N_{\text{part}} = 382$, we introduce systematic error owing to our choice of the functional form of Eq. (A2). To account for this effect, we multiply the error of K^*/K by 2 (1.5) in the most (second-most) central bin we analyze as indicated by the shaded area in Fig. 7. As seen in Fig. 6, we also extrapolate Ω , Ξ , but we do not believe that this adds to the already significant error, considering that our power law interpolation functions describe other hadron yields up to $N_{\text{part}} = 382$.

- [1] P. Bozek and I. Wyskiel-Piekarska, *Phys. Rev. C* **85**, 064915 (2012).
- [2] M. Rybczynski, W. Florkowski, and W. Broniowski, *Phys. Rev. C* **85**, 054907 (2012).
- [3] W. Broniowski and W. Florkowski, *Phys. Rev. Lett.* **87**, 272302 (2001).
- [4] G. Torrieri, S. Steinke, W. Broniowski, W. Florkowski, J. Letessier, and J. Rafelski, *Comput. Phys. Commun.* **167**, 229 (2005); G. Torrieri, S. Jeon, J. Letessier, and J. Rafelski, *ibid.* **175**, 635 (2006).
- [5] B. Abelev (ALICE Collaboration), [arXiv:1209.3285](https://arxiv.org/abs/1209.3285) [nucl-ex].
- [6] B. Abelev *et al.* (ALICE Collaboration), *Phys. Rev. Lett.* **109**, 252301 (2012).
- [7] J. Letessier and J. Rafelski, *Phys. Rev. C* **59**, 947 (1999).
- [8] J. Letessier and J. Rafelski, *Int. J. Mod. Phys. E* **9**, 107 (2000); J. Rafelski and J. Letessier, [arXiv:nucl-th/9903018](https://arxiv.org/abs/nucl-th/9903018).
- [9] J. Letessier and J. Rafelski, *Camb. Monogr. Part. Phys. Nucl. Phys. Cosmol.* **18**, 1 (2002).
- [10] J. Rafelski, J. Letessier, and G. Torrieri, *Phys. Rev. C* **72**, 024905 (2005).
- [11] J. Letessier and J. Rafelski, *Eur. Phys. J. A* **35**, 221 (2008).
- [12] M. Petran, J. Letessier, V. Petracek, and J. Rafelski, *Acta Phys. Pol. B Proc. Suppl.* **5**, 255 (2012).
- [13] F. Becattini, M. Bleicher, T. Kollegger, M. Mitrovski, T. Schuster, and R. Stock, *Phys. Rev. C* **85**, 044921 (2012).
- [14] P. Braun-Munzinger, D. Magestro, K. Redlich, and J. Stachel, *Phys. Lett. B* **518**, 41 (2001).
- [15] F. Becattini, P. Castorina, A. Milov, and H. Satz, *Eur. Phys. J. C* **66**, 377 (2010).
- [16] F. Becattini, J. Manninen, and M. Gazdzicki, *Phys. Rev. C* **73**, 044905 (2006).
- [17] P. Braun-Munzinger, K. Redlich, and J. Stachel, in *Quark Gluon Plasma 3*, edited by R. C. Hwa and Xin-Nian Wang (World Scientific, Singapore, 2004), pp. 491–599.
- [18] A. Andronic *et al.*, *Nucl. Phys. A* **837**, 65 (2010).
- [19] J. Rafelski, *Phys. Lett. B* **262**, 333 (1991).
- [20] J. Rafelski, J. Letessier, and A. Tounsi, *Acta Phys. Pol. B Proc. Suppl.* **27**, 1037 (1996).
- [21] L. P. Csernai, M. I. Gorenstein, L. L. Jenkovszky, I. Lovas, and V. K. Magas, *Phys. Lett. B* **551**, 121 (2003).
- [22] L. P. Csernai and I. N. Mishustin, *Phys. Rev. Lett.* **74**, 5005 (1995).
- [23] J. Rafelski and J. Letessier, *Phys. Rev. Lett.* **85**, 4695 (2000).
- [24] G. Endrodi, Z. Fodor, S. D. Katz, and K. K. Szabo, *J. High Energy Phys.* **04** (2011) 001.
- [25] A. Bazavov *et al.*, *Phys. Rev. D* **85**, 054503 (2012).
- [26] O. Philipsen, *Prog. Part. Nucl. Phys.* **70**, 55 (2013).
- [27] S. Borsányi, *Nucl. Phys. A* **904-905**, 270c (2013).
- [28] M. Ivanov (ALICE Collaboration), *Nucl. Phys. A* **904-905**, 162c (2013).
- [29] B. Abelev *et al.* (ALICE Collaboration), [arXiv:1301.4361](https://arxiv.org/abs/1301.4361) [nucl-ex] [Phys. Rev. C (to be published)].
- [30] B. Abelev *et al.* (ALICE Collaboration), [arXiv:1303.0737](https://arxiv.org/abs/1303.0737) [hep-ex] [Phys. Rev. C (to be published)].
- [31] S. Singha (ALICE Collaboration), *Nucl. Phys. A* **904**, 539c (2013).
- [32] D. D. Chinellato (ALICE Collaboration), [arXiv:1211.7298](https://arxiv.org/abs/1211.7298) [hep-ex].
- [33] A. G. Knospe (ALICE Collaboration), *J. Phys. Conf. Ser.* **420**, 012018 (2013).
- [34] B. Abelev *et al.* (A. Large Ion Collider Experiment Collaboration), *Phys. Lett. B* **712**, 309 (2012).
- [35] M. Petrání and J. Rafelski, *Phys. Rev. C* **88**, 021901(R) (2013).
- [36] M. M. Aggarwal *et al.* (STAR Collaboration), *Phys. Rev. C* **84**, 034909 (2011).
- [37] B. I. Abelev (STAR Collaboration), *Science* **328**, 58 (2010).
- [38] M. J. Fromerth, I. Kuznetsova, L. Labun, J. Letessier, and J. Rafelski, *Acta Phys. Pol. B Proc. Suppl.* **43**, 2261 (2012).
- [39] H. Z. Huang and J. Rafelski, *AIP Conf. Proc.* **756**, 210 (2005).
- [40] J. Rafelski and J. Letessier, *J. Phys. G: Nucl. Part. Phys.* **36**, 064017 (2009).
- [41] J. Rafelski and J. Letessier, *Phys. Rev. C* **83**, 054909 (2011).
- [42] I. A. Karpenko, Y. M. Sinyukov, and K. Werner, *Phys. Rev. C* **87**, 024914 (2013).
- [43] R. Rapp and E. V. Shuryak, *Phys. Rev. Lett.* **86**, 2980 (2001).
- [44] Y. Pan and S. Pratt, [arXiv:1210.1577](https://arxiv.org/abs/1210.1577) [nucl-th].
- [45] F. Becattini, M. Bleicher, T. Kollegger, T. Schuster, J. Steinheimer, and R. Stock, [arXiv:1212.2431](https://arxiv.org/abs/1212.2431) [nucl-th].
- [46] J. Steinheimer, J. Aichelin, and M. Bleicher, *Phys. Rev. Lett.* **110**, 042501 (2013).
- [47] C. Amsler, *Rev. Mod. Phys.* **70**, 1293 (1998).
- [48] W. Brueckner *et al.*, *Z. Phys. A: At. Nucl.* **335**, 217 (1990).
- [49] J. Beringer *et al.* (Particle Data Group Collaboration), *Phys. Rev. D* **86**, 010001 (2012).
- [50] I. Kuznetsova and J. Rafelski, *Eur. Phys. J. C* **51**, 113 (2007).
- [51] J. Letessier and J. Rafelski, *Phys. Rev. C* **75**, 014905 (2007).
- [52] J. Rafelski and J. Letessier, *PoS CONFINEMENT* **8**, 111 (2008).
- [53] P. Braun-Munzinger, J. Stachel, J. P. Wessels, and N. Xu, *Phys. Lett. B* **344**, 43 (1995).
- [54] A. Andronic, P. Braun-Munzinger, and J. Stachel, *Nucl. Phys. A* **772**, 167 (2006).
- [55] F. Becattini, M. Gazdzicki, A. Keranen, J. Manninen, and R. Stock, *Phys. Rev. C* **69**, 024905 (2004).
- [56] J. Manninen and F. Becattini, *Phys. Rev. C* **78**, 054901 (2008).
- [57] J. Cleymans, H. Oeschler, K. Redlich, and S. Wheaton, *Phys. Rev. C* **73**, 034905 (2006).
- [58] B. I. Abelev *et al.* (STAR Collaboration), *Phys. Rev. C* **79**, 034909 (2009).
- [59] P. de Forcrand and O. Philipsen, *Nucl. Phys. B* **642**, 290 (2002).
- [60] K. Aamodt *et al.* (ALICE Collaboration), *Phys. Lett. B* **696**, 328 (2011).
- [61] B. Abelev *et al.* (ALICE Collaboration), [arXiv:1307.5530](https://arxiv.org/abs/1307.5530) [nucl-ex].
- [62] B. Abelev *et al.* (ALICE Collaboration), [arXiv:1307.5543](https://arxiv.org/abs/1307.5543) [nucl-ex].